MOLECULE SPECIFIC CONTRAST USING ULTRA-LOW-FIELD MAGNETIC RESONANCE IMAGING

A Thesis

Presented to

The Faculty of the Department of Chemistry

University of Houston

In Partial Fulfillment

of the Requirements for the Degree

Master of Science

---

by

Vasudeva R.Chintamsetti

August 2013

MOLECULE SPECIFIC CONTRAST USING ULTRA-LOW-FIELD MAGNETIC RESONANCE IMAGING

Vasudeva R. Chintamsetti

APPROVED:

Dr. Shoujun Xu, Chairman
Dept. of Chemistry

Dr. Ding-Shyue Yang
Dept. of Chemistry

Dr. Ognjen Miljanic
Dept. of Chemistry

Dr. Donna W. Stokes
Dept. of Physics

Dean, College of Natural Sciences and Mathematics

MOLECULE SPECIFIC CONTRAST USING ULTRA-LOW-FIELD MAGNETIC RESONANCE IMAGING

An Abstract of a Thesis

Presented to

The Faculty of the Department of Chemistry

University of Houston

In Partial Fulfillment

of the Requirements for the Degree

Master of Science

---

by

Vasudeva R.Chintamsetti

August 2013

Abstract

Optically detected atomic magnetometers use the coherent precession of polarized atomic spins to detect and measure magnetic fields. Low-field MRI using atomic magnetometers with improvements in the spatial resolution and sensitivity can be made more competitive with conventional MRI systems. In the present thesis we report the improvement of spatial resolution of low-field MRI, contrast imaging generated by ligand-conjugated magnetic particles and improvements in selective polarization technique.

Magnetic resonance imaging (MRI) in an ultra-low magnetic field usually has poor spatial resolution compared to its high-field counterpart. The concomitant field effect and low signal level are among the major causes that limit the spatial resolution. Here, we report a novel imaging method, a zoom-in scheme, to achieve a reasonably high spatial resolution of 0.6 mm × 0.6 mm without suffering the concomitant field effect. This method involves multiple steps of spatial encoding with gradually increased spatial resolution but reduced field-of-view. We also demonstrate the use of a unique gradient solenoid to improve the efficiency of optical detection with an atomic magnetometer. The enhanced filling factor improved the signal level and consequently facilitated an improved spatial resolution. Ultra-low-field magnetic resonance imaging usually cannot provide chemical information, because of the loss of chemical shift information. By using ligand-conjugated magnetic particles, we show contrast imaging corresponding to the

particles binding their specific molecular target. A 10% signal decrease was observed when the streptavidin-biotin bonds were formed between the magnetic particles and the surface. Our method provides a unique approach for probing molecules on surfaces, especially under opaque conditions where optical-based imaging techniques are not applicable. The last part of our study is selective polarization, which is unique advantage of low-field MRI. By selectively pre-polarizing the sample in a specific channel provides significant information for studying flow and mixing behaviour in chemical reactions. For the first time we conducted the selective polarization experiment on two different liquids. By selectively polarizing water, we report a 5% difference in the signal intensity at different flow rates. The improvements mentioned in this thesis can contribute for further developments of low-field MRI.

ACKNOWLEDGEMENTS

I am heartily thankful to my supervising professor, Dr. Shoujun Xu, whose encouragement, guidance and support from the initial to the final level enabled me to develop an understanding of the subject. This would not have been achieved without his patience and support. This research project would not have been possible without the support of Dr. Ognjen Miljanic, Dr. Donna Stokes, and Dr. Jerry Yang. I thank them for their valuable suggestions and comments. I would also like to thank all the faculty and staff of the Department of Chemistry and Biochemistry for their support during my entire stay at University of Houston. I would like to extend my thanks to my fellow group members Lashan, Songtham, Li Yao, Te-Wei, Yi Ting, Qiong-Zheng Hu and my dear friend Julie Burrell. I would like to acknowledge NSF for their financial support for this research.

I would like to dedicate this thesis with profound love and affection to my parents Satya Narayanarao, Usha Rani and my wife Lavanya Rekha. Last but not the least I would like to thank my brother Hari Krishna for his encouragement and support throughout my life.

TABLE OF CONTENTS

LIST OF FIGURES

Chapter 1

1. Introduction

In 1946 Bloch *et al.* [1] and Purcell *et al*. [2] discovered nuclear magnetic resonance (NMR). Until recently, the technique was almost exclusively used for structural analysis in chemistry, and for measurements of magnetic shielding tensors, electric field tensors, and coupling tensors in molecular physics. The concept of using magnetic field gradients for imaging nuclear spins was suggested by Lauterbur [3]. Lauterbur also presented a two-dimensional NMR image of a water-filled object, reconstructed from NMR measurements. These images were obtained in the presence of a linear field gradient with a different direction. NMR diffraction in solid using multiple-pulse line-narrowing sequences was demonstrated by Mansfield and Grannell [4]. They also used applied magnetic field gradient. Mansfield *et al.* also showed that ultra-high-speed imaging can be achieved by using rapid gradient variations with echo planar imaging [5] and subsequently this technique became useful in clinical MRI [6].

Since then, NMR imaging has become an important tool in many diverse applications also in other fields such as geology and material science. It has been used as a probe of structure, dynamics, and reaction in industrial and academic fields, along with scientific research [7]. With the progress in method developments, applications for NMR

imaging of materials have been an ongoing research and many of them are discovered [8].

However, due to line broadening, the NMR technique has a limited ability in studying materials with significant amounts of paramagnetic species. The image distortions were observed in samples possessing high magnetic susceptibility gradients, such as materials with metal components. Small penetration depth is another limitation usually occurred when rf excitation pulses are applied to conducting samples [9]. Besides these artifacts, there are also problems associated with engineering and cost, such as the use of cryogenics and superconducting coils to generate strong magnetic fields, which contributes to the high cost and limits the mobility and availability of the device in remote areas, mostly confining it to a laboratory or hospital environment. The bore of a high-field magnet often poses a limitation to the size of the object [10].

Many techniques for low-field detection have been developed and they include conventional inductive detection, detection using superconducting quantum interference devices (SQUIDs), and detection using optical atomic magnetometers [10].

A significant application of ultra-low-field MRI is the capability to image through metal because of the much greater skin depth of low-frequency radiation. For instance, the skin depth of 2.1 kHz electromagnetic wave, which corresponds to the Larmor frequency of protons at 50 μT, is on the order of 1 cm in typical metals, whereas the skin depth is only a few micrometers for 500-MHz radiation [11]. In addition, magnetically heterogeneous samples can be studied in an ultralow magnetic field because the field distortion induced by the magnetic susceptibility of the sample is proportional to the

magnetic field strength. Furthermore, ultra-low-field MRI offers the advantages of portability and low cost; these advantages allow it to be employed in remote areas and in developing regions. Major challenges for ultra-low-field MRI are poor spatial resolution and molecule specific contrast regardless of the detection technique used. Even though conventional MRI, NMR instruments provides high resolution and chemical information respectively, the aim of this work is to improve the spatial resolution and develop molecule specific contrast for MRI at ultra-low-field. Before going into the developments made in this research, the basic principles of MRI and introduction of various detection techniques will be briefly discussed.

1.1 Basics of MRI

Magnetic Resonance Imaging (MRI) is based on NMR and is fundamentally a quantum-mechanical phenomenon. MRI depends on the spins of nuclei with non-zero spin angular momentum [12]. Nuclear magnetic moment is the magnetic moment or magnetic field generated from the spin of protons and neutrons of a nucleus. In the presence of magnetic field, a nuclear spin tends to align itself in the direction of the applied field. Rather than aligning completely, while rotating in the axis of the main field the nuclear spin positions itself at a particular angle with the magnetic field. This particular rotation of the nuclear magnet is termed as precession. The calculated angular frequency during the process of precession is termed as Larmor frequency (ω_0).

$$\vec{\omega} = -\gamma \vec{B} \quad (1)$$

Here, γ is the gyromagnetic ratio. The Larmor frequency ω can be found in the radiofrequency range for high magnetic fields. Depending on the energy level and upon application of B_0, the spin will assume different orientations as shown in Figure 1.1. The lower energy states have more chance to be populated than the upper state, due to the slight difference in their energy levels. Magnetization (M_0), also called as spin polarization, can be determined based on the number of protons which are aligned either parallel or anti-parallel to the B_0 field. Curie law gives the relation between B_0 and M_0.

$$M_o = N \frac{\gamma^2 h^2 I(I+1)}{3(4\pi^2)kT} B_o \quad (2)$$

Here, I is the spin quantum number, γ is the gyromagnetic ratio for a specific isotope, h is Planck's constant, N is the number of nuclei, T is the temperature, and k is Boltzmann's constant [13].The magnetization is proportional to the number of protons and is the net magnetic moment per unit volume. To describe the exchange of energy in an ensemble of nuclear spins, F. Bloch [14] introduced material-specific phenomenological time constants, T_1 and T_2. By dividing the magnetization in to two components M_z and M_{xy}, where M_z is the parallel and M_{xy} is perpendicular to the external field, Bloch was able to describe the magnetization of the components by an equation, which is similar to the exponential decay.

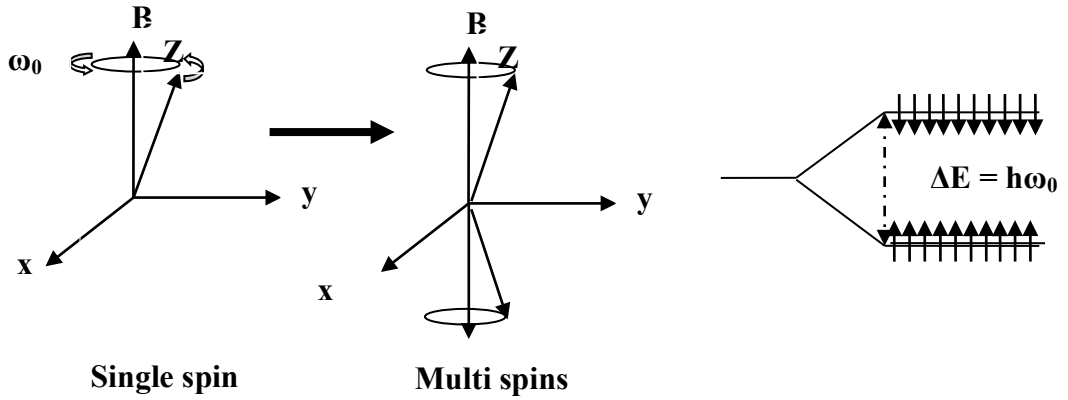

Figure 1.1: Precession of spins in the presence of an external magnetic field, Bo. The frequency of nuclear spin precession is ω_o. In the external magnetic field the magnetic moments align into energy states with the energy difference, ΔE.

1.1.1 Spin-lattice relaxation, T_1

T_1, also called as spin-lattice relaxation is the mechanism by which the magnetization vector along the *z*-axis comes into thermodynamic equilibrium with its surroundings. The T_1 also describes how the magnetization relaxes in the direction parallel to the external field [15].

$$M_z(t) = M_z(0)e^{-\frac{t}{T_1}} + M_0(1 - e^{-\frac{t}{T_1}}) \quad (3)$$

M_z (0) is the starting value and M_0 is the equilibrium value of the magnetization.

The expression determines the time for the spin-flip until the next excitation and it gives information about the time needed to polarize the sample to get largest magnetization.

1.1.2 Spin-spin relaxation, T_2

Within the rotating *xy*-plane, the spin-spin interaction makes the spins dephase. The vectors cancel each other and the total magnetization in the rotating plane consequently decreases. This process can be viewed as if the spins are fanning out. The relaxation rates obey the condition $T_2 < T_1$ [15].

$$M_{xy}(t) = M_{XY}(0)e^{-t/T_2} \tag{4}$$

The spin-spin relaxation time constant, T_2 is the important parameter as it determines the signal acquisition time after a $\pi/2$ pulse. The spin-spin interactions might not be the only cause for dephasing. If there is deviation in the magnetic field (ΔB) over a certain volume of a sample, then different parts will spin with different frequency and is given by, $\Delta f = (\gamma \Delta B)/2\pi$. The dephasing becomes accelerated when the external field is inhomogeneous and the relaxation rate $1/T_2$ can be replaced by $1/T_2^*$. The total dephasing effect can be calculated by separating the extrinsic dephasing caused by the experimental

setup from the intrinsic parameter. The following expression can be used to calculate the total dephasing effect.

$$\frac{1}{T^*_2} = \frac{1}{T_2} + \frac{1}{T_2'} \tag{5}$$

Here, T'_2 is the experimental dephasing. Usually substances exhibit field dependent T_1, T_2 dispersions and T_1, T_2 are shorter at lower magnetic fields. Molecular level dynamics associated with the interactions of the protons can explain the effect of the external field on T_1 and T_2 relaxations. P. A. Bottomley *et al.* [16] did the study of relaxation dispersion on both healthy and pathological tissues. The dispersion data can be explained by the Cole-Cole expression mainly by considering the relaxation rates at low and high-field limits, the transition field amplitude between those values and steepness of transition. Despite of the Cole-Cole expression the dispersion calculation is difficult for some tissues as they exhibit dispersion curves with finer structures. For the tissues containing protein, the nitrogen cross-relaxation dips were found in their relaxation curves [17, 18]. Even though the relaxation dispersion studies were continuing for a long time, the recent findings with water indicate the relaxation mechanism at zero-field limit are still partially unknown [19]. The relaxation of the magnetization and the effect of Larmor precession can be described by the Bloch equation [19, 20, 21].

$$\frac{d\vec{m}}{dt} = \gamma\, \vec{m} * \overrightarrow{B} - \frac{(\vec{m}.\vec{B})\vec{B}}{B^2}\left(\frac{1}{T_1} - \frac{1}{T_2}\right) + \frac{\overrightarrow{\boldsymbol{m^{eq}}}}{T_1} - \frac{\vec{m}}{T_2} \tag{6}$$

MRI is a non-invasive method used to produce images of the interior structure of matter and when compared with other major structural medical imaging technologies, MRI does not include ionizing radiation [22]. Unlike ultrasound imaging, MRI does not suffer from poor penetration through bones [23]. As the sample magnetization and the precession frequency both depend linearly on the magnetic field strength, the induced voltage on a receiving induction coil scales as the square of the field. Accordingly, the field at which MRI performed is above 1-T. Such instruments require heavy solenoidal superconducting magnets to achieve 1-T field and are very expensive. MRI scanners operating at lower fields can be made more open with less cost but have reduced signal strengths. A typical MRI system has a homogenous main field B_0 along the z direction and this field defines a single Larmor frequency. In addition, it uses three linear gradient fields to encode the spatial origin of the signal. A linear gradient field is the magnetic field whose z component varies linearly in one direction and remains constant along the perpendicular directions. Larmor frequency can be made dependent by superposing gradient fields on the main field. The excitation field B_1 at the Larmor frequency is another essential part of MRI systems. It is used to reorient the sample magnetization. π and $\pi/2$ pulses refer to excitation pulses rotating the magnetization vector by 180° and 90°, respectively. The origin of the signals can be decoded by properly controlling the gradient, excitation fields and by acquiring the respective data with induction coils. The signal encoding has to be done so that the image can be reconstructed by Fourier transformation of the measured data. The linear gradient fields can be applied either prior to or during the signal acquisition; the frequency or phase of the magnetic resonance

signal depend on the position [24]. Some other methods use tailored excitation pulses together with the gradient fields to control the flip angle. These encoding methods utilizes only one receiver channel. An array of receiver coils can also be used for signal encoding. The imaging time can be reduced by sampling independent information with several parallel coils [25-26]. By parallel MRI, the idea is to acquire less data per channel than what is required to reconstruct the image with a single-channel receiver. A full image can be reconstructed by sampling partial data in parallel with sensors that have different sensitivity profiles. The improvement in imaging speed and the reduction in the imaging artifacts is possible in parallel MRI [27, 28]. Sensor arrays can also be used to increase the signal to noise ratio. When a combined image is formed, a small coil generates less noise than a large one, thus increases the image SNR [29].

1.2 Ultra-low-field MRI

Ultra-low-field MRI is usually performed in a magnetic field equal or lower than the Earth's magnetic field (~50 μT). The signal strength is reduced when the imaging field is lowered to ultralow magnetic field. Many scientists have been working on the ways to overcome the signal loss at such low field strengths. The sample magnetization can be boosted up by many different ways independently of the main field. This can be done by i) using a pre-polarization field which makes the sample magnetization independent of B_0 [30], ii) detecting the MR signals with sensors having better sensitivity as the performance of induction coils is poor at low-frequencies, and iii) reducing the

external magnetic interference by placing the system inside a magnetically shielded environment. The use of highly sensitive detectors with the combination of pre-polarization fields while the whole system placed inside a magnetic shield was the work first demonstrated in early 2000's [31, 32]. These made possible to image large, room temperature samples in fields as low as 50 μT.

In comparison with conventional high-field MRI, ULF MRI has several advantages. As the broadening of the NMR line width scales linearly with the absolute inhomogeneity of the main field, ULF MRI has fewer requirements for relative field homogeneity [32, 33]. ULF MRI succeeds with simpler coils unlike in high-field MRI that uses sophisticated magnet and a tailored shimming procedure, which are necessary for sufficient field uniformity. Susceptibility differences within the sample in ULF MRI will cause very less distortion than that in the high fields [34]. Due to the spatial variations in magnetic susceptibility, local magnetic field gradients were produced and this causes a significant NMR line broadening at high magnetic fields. Image distortions may be observed due to spatially inhomogeneous broadening. As the local field gradients are reduced together with the applied magnetic field strength, susceptibility variations are typically not a problem in ULF MRI. Thus, the imaging of lung, frontal sinuses and many biological tissues may be easier at ultra-low-fields. In high-field MRI because of the use of metals, the penetration of high frequency electromagnetic fields through conductive material is very poor. Therefore, the use of metal can obstruct MRI at high fields. In contrast the MRI signals an easily be acquired through metallic cans at ultra-low-fields [35]. As the forces on coil structures are weak due to the use of low magnetic fields, ULF

MRI can be considered more silent than the high-field MRI. In addition, ULF MRI can be considered safe as it uses very low magnetic fields, which can allow potentially new patient groups, *e.g.,* people with various metallic implants, to enter the scanner. In comparison with the weight and design, the ULF MRI is of very less weight and is convenient to design with open geometry whereas at high fields, a solenoidal main magnet is typically unavoidable because of its size and weight. The MRI at low magnetic fields also allows us to build hybrid devices [36, 37, 38]. It is also convenient for ULF MRI to extend the instrumentation with additional coils. It could be particularly useful for the imaging of current densities or conductivities. When an external current is supplied through an object, the magnetic field inside the sample changes and depends on the spatial distribution of the current. Due to this, there is an alteration in the spin dynamics within the sample and under appropriate conditions, this can be observed in the measured MR signals. Regarding the rotations of the sample or imaging object, in high-field MRI, as the system is sensitive only to the changes in the magnetic field component parallel to the static main field, the imaging of static current densities requires rotations of the object. In ULF MRI due the modified field sequences, it is possible to acquire the complete current density and conductivity information without sample rotations. Along with the relaxation dispersion, the possibility to vary field strengths can also be utilized to extend the range of different contrasts in image [39]. Imaging of edemas and internal bleeding might be possible with the help of relaxation dispersion. While the use of T_1 dispersion in regard with the security applications has increased [40], the additional

information included in relaxation dispersion may help in discriminating between hazardous and safe liquids.

1.3 Low-field detection techniques

MRI has been most widely used and developed as a powerful imaging technique for the diagnostic applications in medicine. Most of the clinical MRI systems involve magnetic fields generated by large superconducting magnets. However, the interest in development of less expensive imagers that can be operated at lower fields is continuing [41]. Issues pertaining to cost, accessibility and cryogenics can be decreased by eliminating the need for superconducting magnets and cryogenics. In low field MRI the detection can be achieved by different schemes like inductive detection, SQUID, and optical atomic magnetometry. These techniques will be discussed and compared in this section.

1.3.1 SQUID

Superconducting quantum interference devices (SQUIDs) is based on Josephson tunneling effect and is used to measure extremely small variations in magnetic flux. SQUID system consists of one or two Josephson junctions, which interrupts the voltage oscillation of the superconducting loop for the rf and dc SQUIDs. The SQUID converts a flux-to-voltage in which the output of its oscillating voltage is a function of the input magnetic flux [42, 43]. Unlike conventional inductive coils, in SQUID the sensitivity is

independent of magnetic field strength because of which it is possible to achieve high signal-to-noise ratios in very low magnetic fields. This makes possible the NMR and MRI investigations at low magnetic fields [44]. SQUIDs have reached sensitivities below 1 ft/$(Hz)^{1/2}$, sufficient for NMR studies [45]. As the greater portion of NMR studies using SQUIDs have been conducted at liquid helium temperature, the applicability of SQUID has been prohibited to areas where cryogenics are not readily available. The research has been improving to expand the applications of SQUID in NMR and MRI to samples at room temperature. Seton *et al.* improved SQUID and obtained images at room temperature using their apparatus [46]. A one-dimensional NMR image of a sample consisting of mineral oil and tap water at room temperature was obtained by Kumar *et al.* NMR spectra of liquids in fields of a few microtesla were obtained by McDermott *et al.* Möβle *et al.* used their SQUID-detected MRI system to obtain images of objects that cause susceptibility artifacts and rf screening. During their process of investigation of the effects of these objects, they obtained low field images of a phantom grid filled with water, with a titanium bar inside. The imaging of these objects was also done in high-field conditions. Their results indicate that the images at the low field showed less distortion by the titanium bar than at the high field, where images of the phantom within the metal enclosure were not obtained. Another aspect of research is the enhancement of T_1 contrast in low field, which is also one of main reasons for the continued interest in low field. Lee *et al.* demonstrated this by obtaining images of tubes filled with 0.25 % and 0.5 % of agarose solution in the range of 10μT to 300 mT. The observed difference is with the contrast of the images where it is much stronger in images obtained in lower

fields; conversely, there is virtually no contrast at a higher field [47]. Direct detection using SQUID system simplifies the measuring procedure, and even works with reduced field homogeneity [48]. The high sensitivity and flexibility of SQUIDs enables the detection of NMR and MRI in microtesla magnetic fields. At frequencies ranging from zero to several GHz, it has a broad range of applications [49]. The use of cryogenics and complex electronic components for arrayed SQUIDs limits the portability and availability [48].

1.3.2 Atomic magnetometry

Another alternative detection method for low-field NMR is atomic magnetometry. This technique can be considered as one of the most sensitive techniques used to measure dc magnetic fields [45]. Kastler [53] suggested the use of optical techniques to produce magnetic polarization of electrons in a vaporous sample and the development of optically pumped scalar magnetometers have progressed. Dehmelt *et al.* suggested the method of detecting magnetic resonance by modulating the Larmor frequency of a light beam placed at right angles in a magnetic field [49]. Later Bell and Bloom designed an apparatus in which resonance signals have been observed in optically pumped sodium. The possible applications have also been suggested [50]. Parsons and Wiatr [51] developed an ^{85}Rb magnetometer employing the optical pumping technique. This magnetometer is used to record continuous variations in the Earth's magnetic field. A low-field magnetometer that was used to detect static magnetic field produced by optically pumped ^{3}He nuclei was developed by Cohen-Tannoudji *et al.* [52] in which ^{3}He nuclei was placed in 6 cm

diameter cell, allowing the study of its nuclei polarization. Atomic magnetometers have been receiving a lot of attention after the progress of this technique. Savukov *et al.* [54] first demonstrated the detection of NMR spin precession signal from a thermally polarized water sample using a non-cryogenic spin-exchange-relaxation-free potassium magnetometer. The NMR signal, which determines the NMR frequency, is present in a solenoid. To detect the proton signals Savukov *et al.* demonstrated an RF atomic magnetometer, which was tuned to a frequency of 62 kHz. The detection scheme engages a static water sample in a cell. The water sample was pre-polarized using either pulsed magnetic field or permanent magnet. For the purpose of detection, the cell was positioned in a closely wrapped long solenoid [54]. There is ongoing research to minimize the size of the setup, complexity and increase the performance of atomic magnetometers. Xu *et al.* developed an optical atomic magnetometer based on the rotation of ^{87}Rb vapor in 1 cm cells [55]. This work is suited for the application of remote detection for NMR and MRI. Balabas *et al.* constructed a small, low-power atomic magnetometer using mm-scale ^{87}Rb cells and demonstrated the efficiency and sensitivity of millimeter scale atomic magnetometers [56]. Shah *et al.* demonstrated the feasibility of the use of a magnetometer based on a micro machined 6mm alkali vapor cell [87]. This system uses a simplified optical configuration that makes use of a low-power laser and has sensitivity below 70 fT/Hz$^{1/2}$. Balabas *et al.* [57] indicated that 3 mm cells as the appropriate size for small-scale magnetometers, they also verified that the Zeeman-relaxation rate's dependence on the characteristic dimension of the cell, D, is 1/D. Their results show the potential of mm-scale cells in the development of small-scale magnetometers. These

developments have allowed atomic magnetometers to compete with SQUID-based magnetometers, which have been leading in sensitivity for a number of years [58]. The salient features of atomic magnetometers were sensitivity, weight, power, cost and reliability. These features determine their ability to carry out certain applications. The use of tunable diode lasers and the absence of cryogenics were some of the critical advantages developed in the new techniques. These changes drastically reduce the size as well as power consumption. Overcoming these limitations increased the opportunity and possibility for the applications of these atomic devices.

1.3.2.1 Principle of Atomic magnetometry

Optical atomic magnetometry is based on the magneto-optical interactions of a laser beam with spin-polarized atoms of an alkali vapor in the presence of a magnetic field [54]. A schematic is shown in Figure 1.2. The source of light is a polarized laser beam with a frequency at or near the resonance of one of the optical transitions of the alkali atoms. The polarized laser has been used to generate a coherent population with the atomic ground state in the alkali vapor that is enclosed in a glass cell. The interaction of the spin-polarized alkali atoms with the laser beam consequently results in an optical rotation of the polarization of the laser beam or a dispersive absorption spectrum.

The optical properties of modulated probe beam are a measurement of the magnetic field to be detected. The magneto-optical effects depend on the magnetic field applied to the atoms, either from a calibration coil or introduction of the sample or both.

This magnetic field causes Zeeman splitting in the electronic states of the alkali atoms. The detection of the magnetic field is dependent on the detection of photons [48].

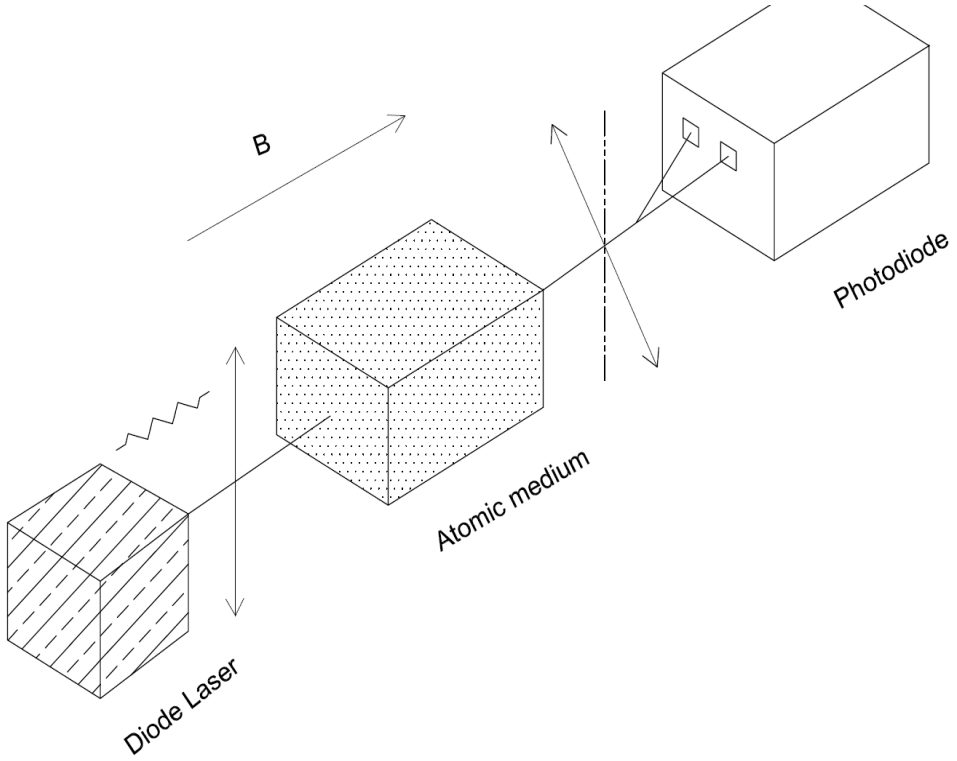

Figure 1.2: Schematic representation of atomic magnetometer. Magnetometer measures the polarization rotation of the laser light that interacts with the atomic medium, which is an alkali vapor, in the presence of a magnetic field.

1.3.2.2 Faraday Effect

Many research groups have discussed the effects of light over a sample in nuclear magnetic resonance (NMR) experiments. The magneto-optical phenomenon delivers novel, sensitive methods for detection in NMR. The Faraday Effect has to be considered when discussing nuclear spin optical rotation (NSOR). In the Faraday Effect, the magnetic field due to spin-polarized nuclei causes the rotation of the plane of polarization of an incident beam of linearly polarized light. On the other hand, circularly polarized light induces shifts in NMR frequencies in the inverse Faraday Effect. Michael Faraday was the first to present the experimental evidence of the interaction of light and magnetic field in a medium. By using a light source, polarizer, polarimeter, and medium in the presence of magnetic field, he demonstrated that upon interaction of light with the magnetic medium, the plane of polarization of light rotated by an angle proportional to the magnetic field.

The Faraday Effect can be explained by considering the linearly polarized light as a superimposition of two circularly polarized components. The conversion of the circular components to the Cartesian coordinates can be done by using the following equations.

$$\hat{E}_x = \frac{1}{\sqrt{2}}\left(\hat{E}_+ + \hat{E}_-\right) \tag{7}$$

$$\hat{E}_y = \frac{-i}{\sqrt{2}}\left(\hat{E}_+ + \hat{E}_-\right) \tag{8}$$

where, $\hat{E}_x$ and $\hat{E}_y$ are the unit vectors representing light polarized along x and y respectively. $\hat{E}_+$ and $\hat{E}_-$ are the vectors representing right and left circularly polarized light. If the light is polarized along y- axis and the wave vector k propagates along z, then electric field vector E can be written as

$$E = E_0 \hat{E}_y \cos(kz - \omega t) \quad (9)$$

$$E = \frac{\iota E_0}{2\sqrt{2}} \left(\hat{E}_+ e^{-\iota(kz-\omega t)} - \hat{E}_- e^{-\iota(kz-\omega t)} \right) + c.c., \quad (10)$$

where, E_0 is the amplitude of the electric field, ω is the frequency of the light, and c.c. is the complex conjugate. The wavenumber k, is given as

$$k = \frac{2\Pi}{\lambda} = \frac{\eta\omega}{c} \quad (11)$$

where λ is the wavelength of light and η is the complex refractive index and is given as,

$$\eta = n + \iota\kappa \quad (12)$$

The refractive index *n* is the real part of the complex refractive index. This is associated to the dispersion of the medium. The imaginary part is given by the absorption coefficient κ. There is a difference in the phase of a beam when $n_+ \neq n_-$, and each component travels at a different velocity. This can be explained by the equation

$$\varphi = \frac{\omega l}{c}(n_+ - n_-) \quad (13)$$

where φ leads to rotation of plane polarization by an angle ϕ

$$\phi = \frac{\varphi}{2} (14)$$

The change in refractive indices is caused by the magnetic field.

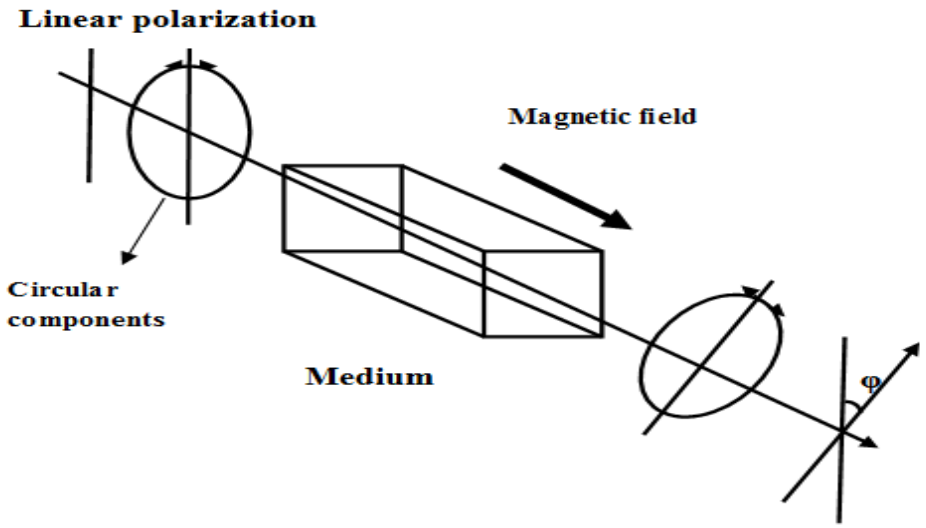

Figure 1.3: Linear Faraday Effect. When light impinges on a medium in the magnetic field, the polarization is rotated by an angle φ.

In simple when light propagates through an atomic sample along the direction of a magnetic field and is tuned to the vicinity of an atomic resonance, the plane of light polarization will be rotated at the output of the medium. If the light intensity is sufficiently high so that the atomic transition begins to saturate, several nested, dispersive-shaped features can be observed, and the rotation angle is maximum at the low magnetic field. These features are non-linear magneto-optical rotation (NMOR) resulting from a modification of the optical properties of the atomic medium by the light field via

optical pumping. Non-linear magneto-optical rotation and closely related phenomena has been the subject of extensive experimental and theoretical work for many decades, as discussed in detail in the extensive review.

1.3.2.3 Non-linear magneto optical rotation

Non-linear magneto optical rotation (NMOR) is a process that depends on the intensity of polarized light that propagates through the medium in a magnetic field. In 1974 Gawlik and co-workers first measured NMOR using laser. They found that the NMOR signals as a function of magnetic field had a distinct feature. When compared to the Doppler-broadened linear magneto-optical rotation (LMOR) signal, the new signal was narrower and the rotation of polarization plane depended on the light intensity. A non-linear optical condition can be achieved by saturating the upper state energy level. This can be achieved by optical pumping. Near resonance the saturation parameter is a useful tool to describe the non-linear process. The saturation parameter κ can be expressed as,

$$\kappa = \frac{excitation\ rate}{relaxation\ rate} \tag{15}$$

In the condition where κ_1 is less than 1 then the domination of the spontaneous emission can be observed and lower sublevels are mostly populated. In the case where κ_1 is greater than 1 , the atoms experience regular Rabi collisions which is cyclic absorption

and emission of photons. This occurs at a much faster rate than spontaneous emission and the average population of the upper and lower states become equal. Usually non-linear processes are known to occur using high intensity beams. It was also known from earlier studies that this can happen using weak powered light from conventional spectral lamps. In NMOR process both the properties of the medium and light are changed. Optical pumping can change the atomic population and optical probing can change the polarization of light. Both the optical pumping and optical probing can be done using a single beam. The mechanisms can only be understood by using two separate beams. Barkov and co-workers identified two prmary mechanisms behind NMOR. They were the Bennett-structure formation and Zeeman coherences. Between these two effects the primary determining factor is the magnitude of the magnetic field B_{max}. At this B_{max} the rotation is considered to be maximum. It is also related to the line width Γ in the following expression.

$$B_{max} = \frac{\hbar \Gamma}{2g\mu} \tag{16}$$

According to the Bennett-structure effects, the smallest linewidth that can be obtained corresponds to the natural width of atomic transition. On the other hand for coherence effects, line width depends on the rate of atomic depolarization. Optical rotation is found to be greater with the coherence effects than that of Bennett-structure effects. Another team involving Barov *et. al.* [58] observed greater optical rotation with coherence effects than linear Macaluso-Carbino effect by a factor of 10^4. Considering these studies, anything that destroys coherence and accordingly the over-all spin

polarization, has a major effect on the magneto optical signal being measured. While measuring rotation, if the modulation is not present, the sensitivity of the polarimeter is limited by the low-frequency noise. This can be adjusted by some form of fast modulation. The polarization modulator can reduce the sensitivity of polarimeter to lower the frequency noise. But still, it is sensitive to drifting signal which is detected from changes between relative rotation of polarizer and analyzer. This can also be the signal which is detected from the alteration in the birefringence of optical elements. This signal is similar to the signal due to optical rotation from atoms and cannot be distinguished. Frequency modulation technique can be used to overcome this drawback [59]. Faraday modulator and other optical elements were not needed. The piezo actuator of a diode laser is modulated in frequency modulation technique. As the frequency of laser is modulated, the rate of optical pumping differs with the laser detuning from the transition. The change in the optical pumping rate occurs periodically as modulated by the modulation frequency ω_m. The atomic polarization which depends on the magnetic field also changes periodically. The change occurs at a frequency equal to $2\omega_L$ only when the atomic polarization alignment is ransverse to the magnetic field. If the periodicity of the optical pumping happens to synchronize with Larmor percession, a resonance is observed and the atoms were pumped in to aligned states rotating at ω_L. This leads to dispersive resonances in optical rotation detected as the signal. Using amplitude modulated light is the alternative of using frequency-modulated light. Gawlik *et al.* [60] and Balabas *et al.* [56] were the first to perform experiments with amplitude-modulated light. Macroscopic polarization of a medium can be generated using amplitude-modulated light. This occurs

when the frequency of light modulated is synchronized with the Larmor precession. Depending upon the periodic changes of the light intensity the pumping rate is modulated. At zero magnetic field and at higher magnetic field this methods can produce ultra-narrow resonances. Therefore the applications can be extended for magnetic fields ranging from the microgauss level to the earth field with sensitivity up to 10^{-11} G/Hz. Atomic modulated light minimizes the deformation resulting from spurious atomic modulation of laser light and the ac Stark-effect shifts. In the situation where it is difficult to change the light-source frequency, the NMOR with atomic modulation can be used and it provides additional parameters in optimizing the modulation wave for better control of dynamics. The intrinsic sensitivity of the atomic magnetometer is given as,

$$\delta B = \frac{1}{\gamma\sqrt{N\tau t}} \quad (17)$$

where γ is the gyromagnetic ratio, N is the number of atoms, τ is the coherence lifetime, and t is the measuring time. Coherence lifetime is the time the spins maintain their polarization in the absence of pumping. The coherence lifetime and density of atoms are the main factors affecting the sensitivity of a magnetometer.

1.3.3 Nitrogen-vacancy diamond magnetometry

Even though atomic magnetometers without cryogenics have the ability to measure magnetic fields with exceptional sensitivity, spin-altering collisions limit the sensitivity of sub-millimeter-scale sensors [62].Consequently, it is challenging to achieve

spatial resolution beyond millimeter regime. Magnetic measurements using SQUIDs [19, 48] as well as magnetic resonance force microscopes (MRFMs) have been in process to probe magnetic fields with nanometer resolution. Nonetheless, the best spatial resolution of the SQUID sensors is still not significantly better than a few hundred nanometers [63]. In addition, SQUIDs require cryogenic cooling to achieve high sensitivity, which limits the choice of possible applications.

The magnetometer with nitrogen-vacancy (NV) centers is a new emerging technique for measuring magnetic fields at the nanometer scale [64, 65, 66]. With a unique combination of spatial resolution and magnetic sensitivity in a wide range of temperatures (from 0 K to well above 300 K), the system offers the possibility to detect magnetic fields opening up new frontiers in biological and condensed matter research. Researchers have developed many schemes for scanning magnetometry using nanoscale-imaging techniques in bulk diamond, as well as in nanometer-sized diamonds combined with scanning probe techniques. Detection techniques, which employ ensembles of NV centers, promise even higher sensitivity and the possibility to map out all vector components of the magnetic field. Recently several groups demonstrated the pilot NV-ensemble magnetometers [67, 68].

In the present work, we used an optically detected atomic magnetometer because of its low cost and high sensitivity (~80 fT$\sqrt{Hz}$). Ultra-low-field (~0.2μT) conditions were maintained at the detection region. Two drawbacks of ultra-low-field MRI has been our main research interest. They are poor spatial resolution and molecule specific contrast. Magnetic resonance imaging (MRI) in an ultra-low magnetic field usually has poor

spatial resolution compared to its high-field counterpart. While the conventional MRI has reported a 3-μm resolution, a 1.2 × 1.2 mm resolution has been reported using MRI at ultra-low-field. The concomitant field effect and low signal level are among the major causes that limit the spatial resolution. The parameter that measures the concomitant field effect is given by $\varepsilon = GL/B_0$, where G is the gradient magnetic field, L is the dimension of the FOV, and B_0 is the leading magnetic field. Our idea is to avoid the concomitant field effect by simultaneous increase in the gradient strength and reduction in the FOV. Based on the above given equation, the zoom-in method keeps ε constant through a simultaneous increase in the gradient and a decrease in the size of the FOV. Low field MRI using atomic magnetometers with improvements in the spatial resolution and sensitivity can be made more competitive with conventional MRI systems. The details of the zoom-in scheme and our contributions to improve the spatial resolution were mentioned in chapter 3 of this thesis.

Nuclear magnetic resonance (NMR) and magnetic resonance imaging (MRI) techniques distinguish them from other spectroscopic techniques by providing detailed chemical shift information and contrast for different environment. When NMR/MRI is performed in an ultra-low magnetic field (ambient field or below), however, it is challenging to maintain these advantages and usually cannot provide chemical information, because of the loss of chemical shift information. MRI images depend on the RF signals arising from the magnetic moments of tissues containing water protons. The advantages of using water protons as the probe molecule were that protons have highest sensitivity among the biologically relevant nuclei. Proton spin density, and

longitudinal (T_1) and transverse (T_2) relaxation times play an important role in the normal contrast of the MR images. A special set of contrast agents called chemical exchange saturation transfer (CEST) agents work by the transfer of magnetization from magnetic particles to water and consequently decreases the water signal intensity. The probing of magnetic nanoparticles to the biological molecules to study the interactions between the particles has been a well-known technique. Magnetic particles also have the ability to decrease the transverse (T_2) relaxation time and can be used in the imaging purposes. The objective of our study is to obtain the contrast from the specific bond between streptavidin coated magnetic particles and biotin coated substrate in ultra-low-field MRI. An attempt to obtain contrast by selectively polarizing one of the heterogeneous liquid samples has been made in the present work. The contrast in the image has been obtained but the quantitative estimation of the difference in the density of the protons is yet to be made. The biological applications of magnetic nanoparticles and the bonding behavior of the streptavidin-biotin complex have been detailed in section 4.2.2 & 4.2.3.

Chapter 2

2. Instrumentation, electronics and communication system

MRI in the low field environment requires strong pre-polarization, encoding region at ambient field, and the detection region at ultra-low-field. The imaging process starts with the pre-polarization of the molecules and ends at the detection region. The detection schemes and the principle of atomic magnetometer were previously discussed in the introduction section. In this section, we discuss the pre-polarization equipment, pulse sequence software, hardware, and experimental setup for the selective polarization experiment.

2.1 Pre-polarization

While performing experiments to image any samples or chemicals, the process starts with the pre-polarization of the sample. There are several techniques used to pre-polarize the sample. They are :

1. Thermal polarization with permanent magnet
2. Thermal polarization with electromagnet

3. Hyperpolarization (for ^{129}Xe and ^{3}He)

4. Para-hydrogen

5. Dynamic nuclear polarization (DNP)

The selection of different methods is based on the type of sample and the detection technique used to obtain the signal. In our experiments we use thermal polarizarion with permanent magnet for pre-polarizing water molecules. As the scheme for the experiment is the remote detection scheme, the pre-polarization, encoding, and detection regions are separated. In order to minimize the field effect from the permanent magnet the whole setup is placed in a shield. The details of the magnet we used and the shield were as follows. We used a RHR-1.95T-10 magnet made of Sintered NdFeB. The total magnetic field at the center is >= 1.95 Tesla (at 20 °C). Figure 2.1 is a photo of the setup used to hold the magnet. The magnet is placed in a wodden casing which is totally covered by a shield. The variation of the magnetic field (in % of the central field value) in the *xy, yz,* and *xz* axes is shown in figures 2.2 (a) & (b). The center part of the pre-polarization magnet (the red dotted area in figure 2.2) where the liquid passes has the maximum magnetic field.

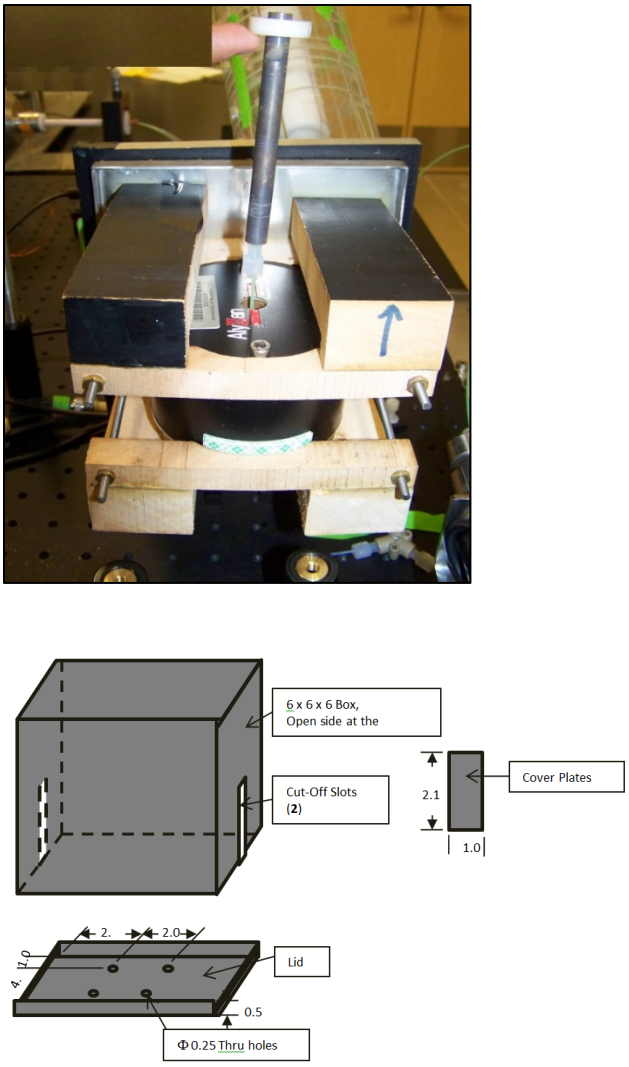

Figure 2.1: On the top is a photo of the described RHR-1.95T-10 magnet placed in a wooden casing. The rod on the top holds the liquid is the place where the polarization occurs. At the bottom is the 0.062 inches thick shield used to shield the magnetic field.

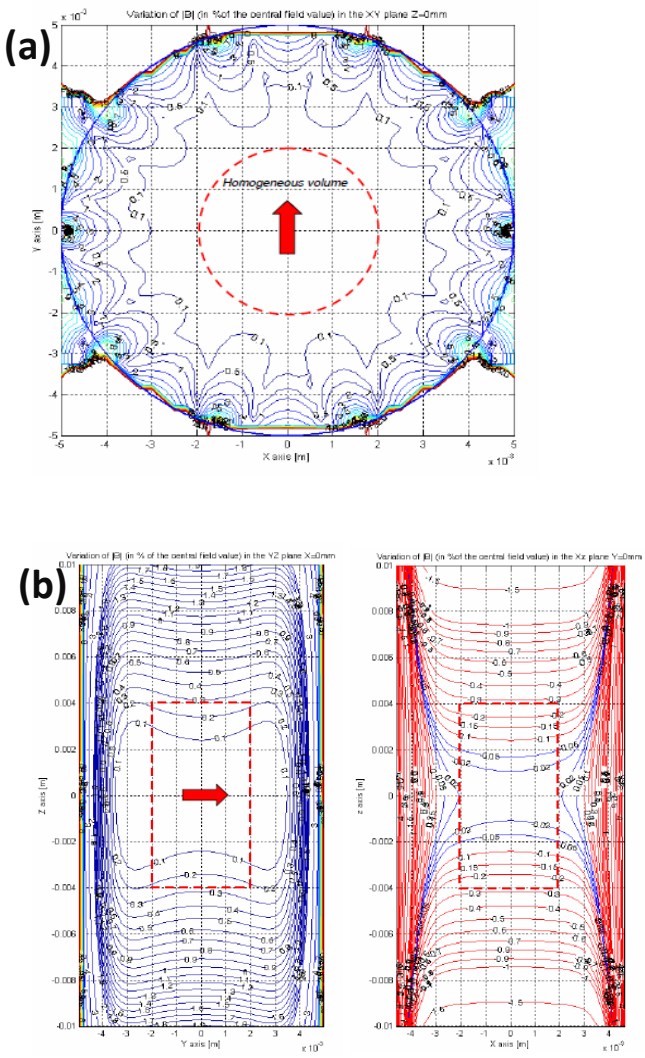

Figure 2.2: Figures (a) showing the variation of magnetic field as % of the central field value in the xy-plane. (b) The image on the left and right showing the variation of magnetic field as % of the central field value in the yz-plane and xz-plane respectively. In the images the red dotted spots is the area of maximum magnetic field.

2.2 Pulse sequences in NTNMR program

In NTNMR the pulse sequences are created, edited, and displayed in a graphical format. The horizontal lines of the pulse sequence correspond to a particular function in the NMR instrument. The columns represent the events in the pulse sequence, which are ordered from left to right. Some of the features of creation and editing of pulse sequence in MTNMR are:

• Sequences can be saved with the data file (*.tnt) format. They can also be saved separately (*.tps) so that they can be used with other data files.

• The sequence tables (phase, delay, shape, etc.) can be created with a built-in text editor of the Edit Table dialog window and can be saved along with the sequence.

• Multi-dimensional tables are maintained as a separate section of the graphical window and these tables can be viewed as icons or table names.

• User defined variables, which appear in the sequence tab of the dashboard, can be used unlimitedly.

The components of the pulse sequence window are:

• Sequence Toolbar (left side of window)

• Line labels (i.e. .F1_Ampl. .Acq., etc.) are associated with various spectrometer functions.

• Event numbers (from left to right across the top of the window).

• Delay line defines the duration of each event in the sequence.

• Grid, the major part of the window containing event icons, indicating the action for each line of the sequence during each event.

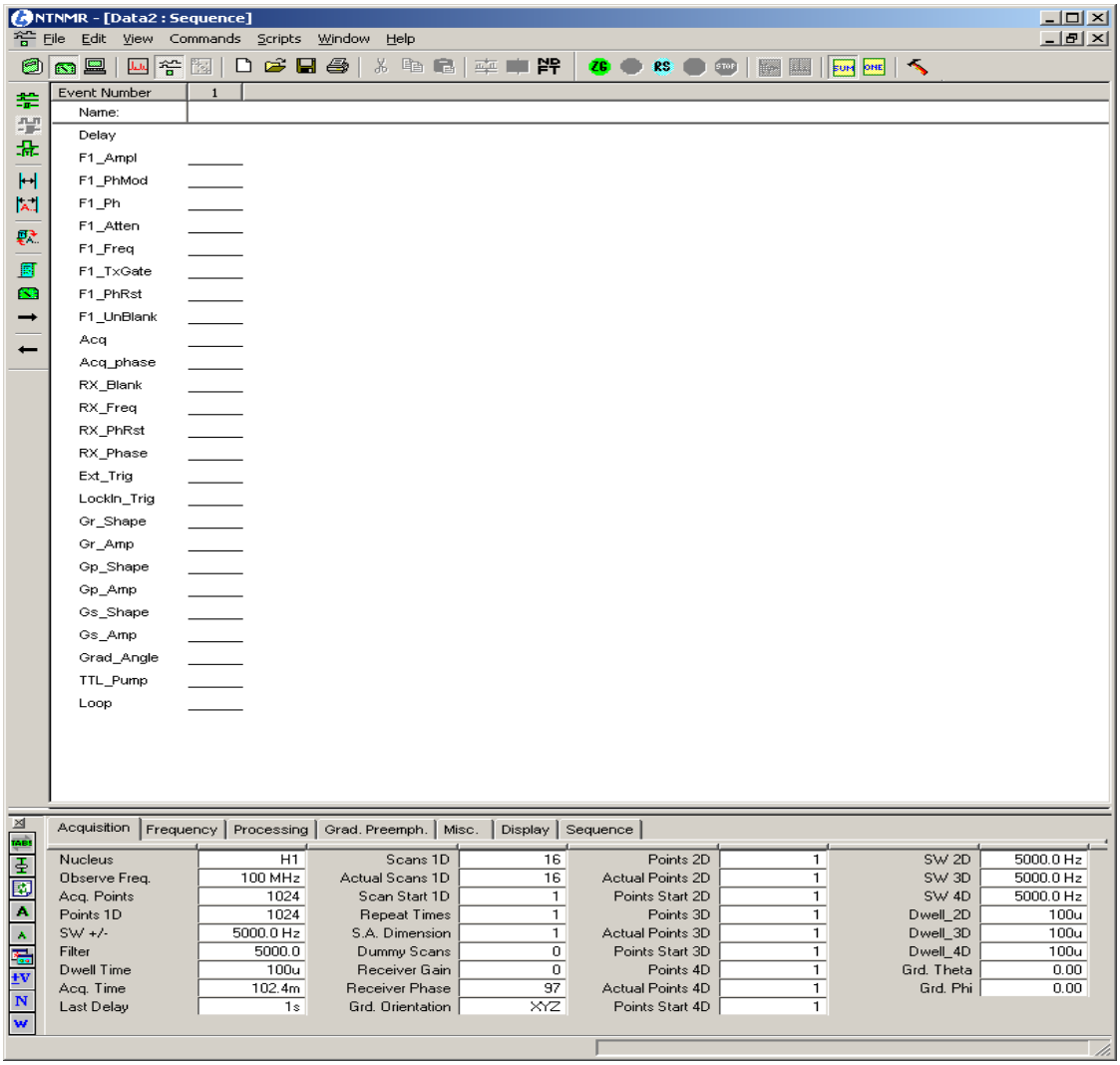

Figure 2.3: The NTNMR interface used to create and control the pulse sequence.

Sequence elements

Each position referred as event in an NTNMR pulse sequence can be thought of as a cell in a spreadsheet representation of a pulse sequence. Its event number and line label determine location of the event. The function of the pulse sequence progresses from left

to right, executing all commands in that event column for a duration defined by the delay for that column. Each line represents a specific spectrometer function, such as RF phase amplitude, acquisition, transmitter gate, gradient size, and so on. The events on the left-hand side in the sample grid (white space) were the sequence elements. In this section concise information about some of the sequence elements is given. The first sequence element is the delay line, which gives information about the duration of each event in the pulse sequence. The transmitter type is one of the sequence element in which the popup menu is generally used for lines that control the transmitter gates belonging to the RF channels on spectrometer. Phase type (PH) is used to control the phase of various RF channels and of the acquisition. The phase usually corresponds to 0, 90, 180, 270 (+X, +Y, -X, -Y). The controls values for this phase information would be 0, 1, 2, 3 respectively. The numbers entered were not phase angles, but rather integer numbers. The acquisition icon denotes the system to begin acquiring data at that event in the sequence. The Gr, Gp, Gs events are useful to carry information about the gradient size and amplitude range for different axes.

During the work in Chapter II, we have used a zoomed-in scheme to identify the sample with thickness up to 0.6 mm. The two main factors determining spatial resolution are the field of view and the matrix size. A zoomed-in image can be obtained by decreasing the field of view. In conventional MRI, the FOV can be decreased by changing the gradient strength and the receiver bandwidth. In the present low field MRI setup, we change the gradient strength, duration of the pulse and the gain. The line spacing in k-space is inversely proportional to the FOV. If there is a decrease in the FOV,

the line spacing in k-space increases. The increase in the spatial resolution occurs by maintaining the same matrix size and increasing the spacing between the lines in k-space. Briefly, the number and size of points composing it determine the spatial resolution of an image. It is inversely proportional to voxel size, the higher the spatial resolution the smaller the voxel size. By diminishing the FOV and maintaining the same matrix, the voxel size goes down and by maintaining the FOV and increase, the matrix the voxel size goes down. If the matrix size is doubled, for instance from 125 × 128 to 256 × 256, the number of voxels goes up by a factor of four and their volumes go down by a factor of 4. Therefore, as the resolution goes up, the voxel size goes down. In our experiment, we have changed certain parameters in the pulse sequence to attain the zoom. The amplitude along the Y-axis is 50% and the gradient size is 18 with 11steps. The duration of the pulse is 10 ms. Screen shot of the pulse sequence we used is shown in figure 2.4.

2.3 Gradient Amplifier

The pulse sequence can control the gradient size, phase information, time of the pulses, etc. The LF1 Apollo unit and the gradient amplifier are the interface between the software and the encoding region. For the NMR/MRI part, a TECMAG system was used to program the various pulse sequences. The excitation pulse was at 2.1 kHz, corresponding to the Larmor frequency in the ambient magnetic field. A two-channel current amplifier for the spatial encoding amplified pulses for the gradient coils. A trigger pulse was generated by the TECMAG to synchronize the MRI encoding with the

detection using the atomic magnetometer. The gain knobs as seen in the figure 2.5b were the actual controls in the amplifier. Gain is a measure of the ability of an amplifier to increase the amplitude of a signal from the input to the output, by adding energy to the signal.

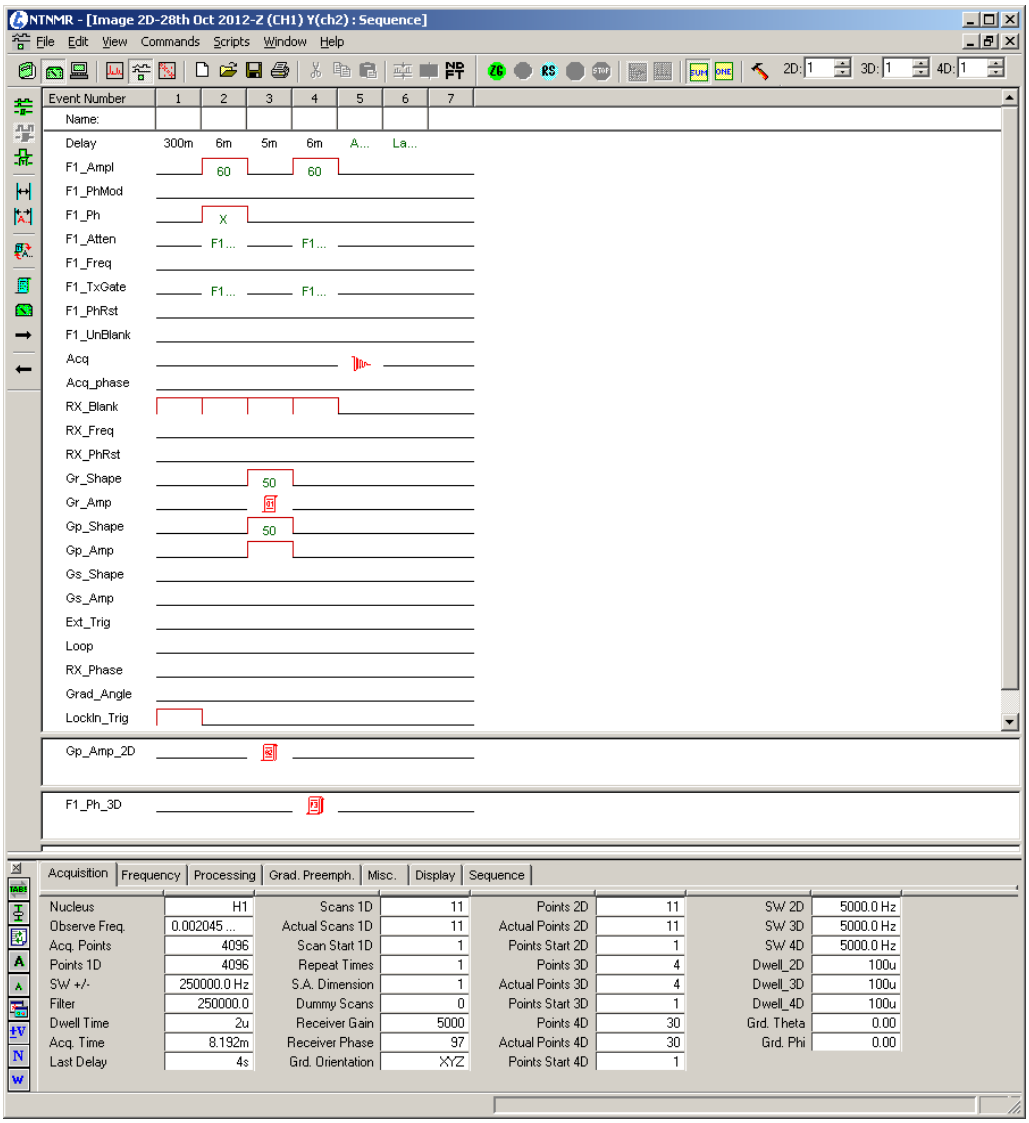

Figure 2.4: The pulse sequence used for the molecule specific contrast MRI experiment

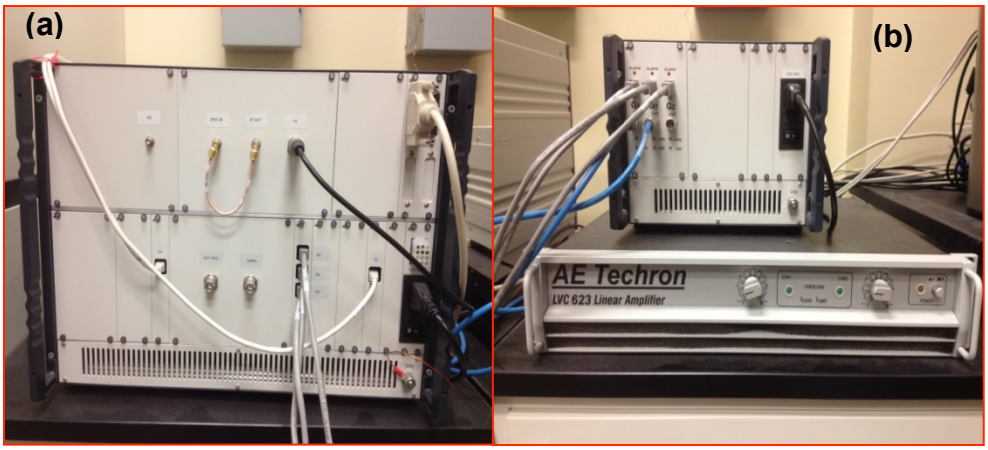

Figure 2.5: Photo of the instrument that generates and transfers the rf pulses. (a) Tecmag LF1 Apollo unit for sending rf pulses. (b) Gradient amplifier from AE Techron.

Figure 2.6 is the flow chart of the electronic connectivity. In order to overcome low-frequency noise, fast modulation of light is necessary. In those cases, lock-in detection has been used. In the research mentioned in this thesis, the differential current signals were measured with a time constant of 50 ms. Lock-in amplifiers were used as voltage source for the piercing solenoid. A function generator provides the modulation frequency to the laser controller. The second amplifier, which is used for the DAVLL system gives the dc signal to lock the laser at a specific wavelength. All information is fed in to the laser controller via an ac-dc mixer.

2.4 Detection region

Ultra-low-field in the detection region can be maintained by using magnetic shield casings. The field inside the magnetic shield was found to be ~0.2 μT. In the work

presented in this thesis, we used a 5×5×5 mm^3 glass cell that contains ^{133}Cs atoms. The inner walls of the cell are paraffin-coated so to minimize relaxation of ground-state polarization due to collisions with the wall. The ^{133}Cs alkali atoms have distinctly resolved absorption bands which reduces the possibility of laser-frequency cross-over. Cs-based atomic magnetometers seemed to be preferred type for common optical magnetometers due to its high accuracy and low heating demands. The construction and development of the MRI systems using atomic magnetometers were described in the previous publications from our group [57]. A brief description of the optical setup is given in this section.

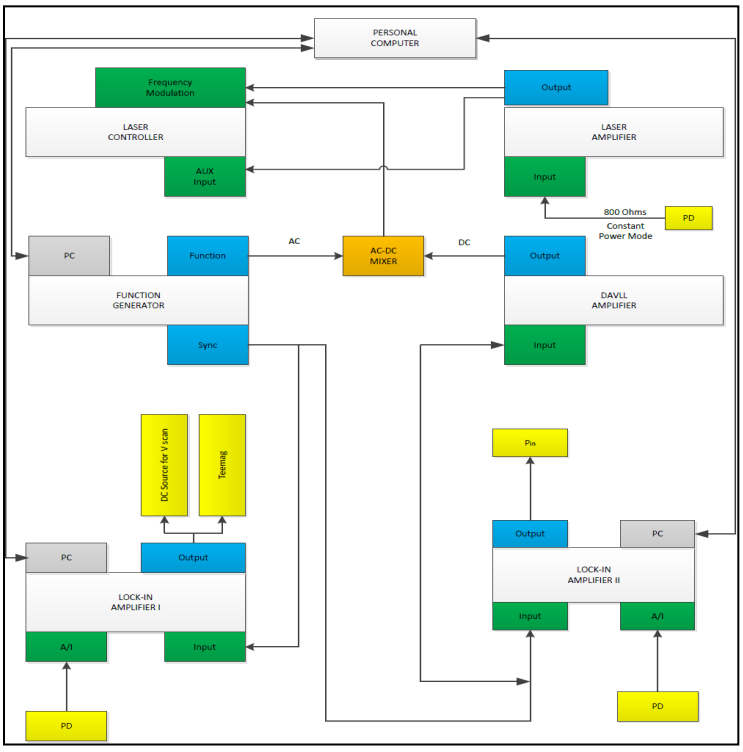

Figure 2.6: Electronics and communication system.

A diode laser (New Focus, model 7018) is used for the magnetometer. The neutral density filters attenuate the beam. A small portion of the laser light is directed towards the dichroic atomic vapor laser lock (DAVLL) to lock the laser at the optimal wavelength. This helps to stabilize frequency of the laser. The reason for this is that there is a drift of the central frequency with change in temperature, current, and mechanical fluctuations. This drift can be reduced by using the DAVLL. This works by generating an electronic feedback signal to control the laser frequency and it locks the laser for long-term signal stability. Locking the laser to the DAVLL signal means to stabilize laser frequency to the zero crossing. By adjusting the quarter-wave plate the frequency lock point can be tuned. The polarization of the outgoing light is determined by a circular analyzer consisting of a quarter-wave plate and the polarizing prism directing the light to two photodetectors. The difference in the intensities of the light going to the two photodetectors is a measure of the optical rotation.

The other portion of the laser is directed through several optical elements and is reflected back through the cells and passes through a polarizing prism. The magneto-optical rotation for each sensor is detected by photodiodes and amplified by a lock-in amplifier (SR830).

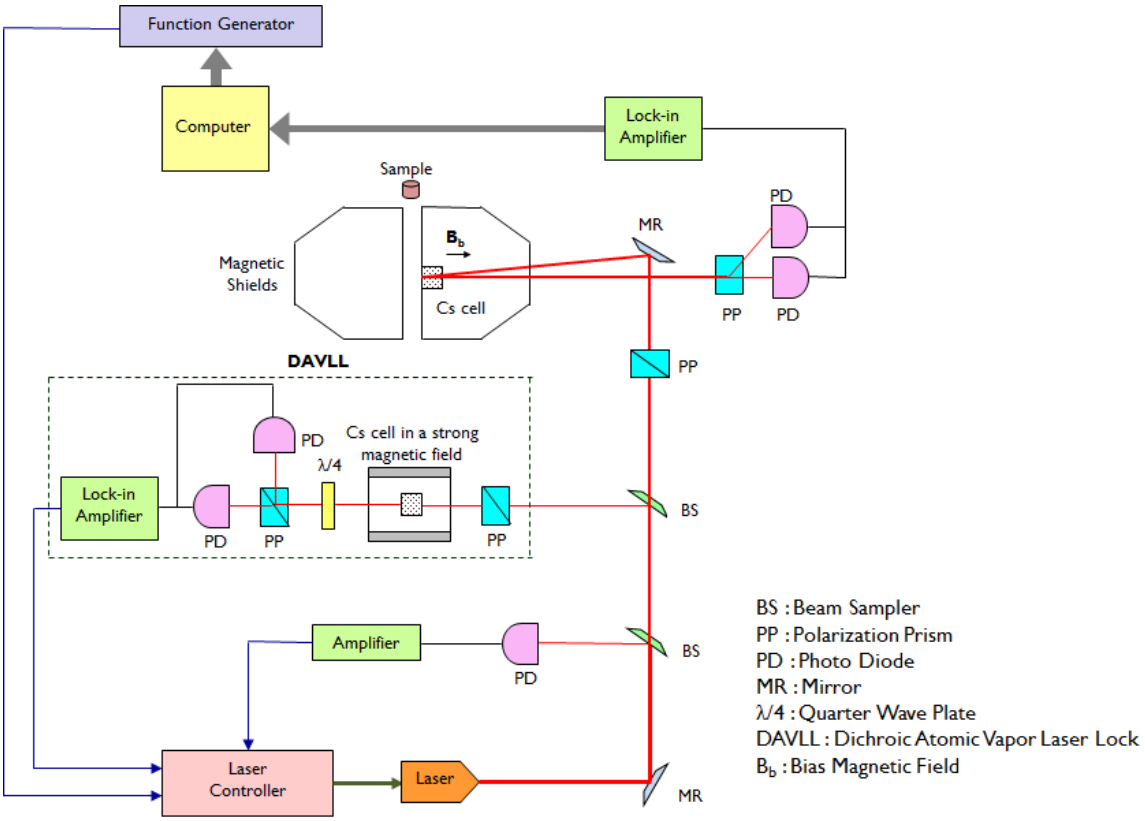

Figure 2.7: Optical layout of the setup used for the optically detected atomic magnetometry.

The LABVIEW program for the dual pump setup and the MATLAB code used for the imaging were described as a separate section in APPENDIX.

Chapter 3

3. Development of spatial resolution in optically detected magnetic resonance imaging

3.1 Motivation of the study

Because of the relatively poor sensitivity of the inductive coils in an ultralow magnetic field, an alternative detection technique is usually used. Several research groups [69-73] have used superconducting quantum interference devices (SQUIDs) for ultra-low-field MRI. Optical detection with atomic magnetometers was later reported for ultra-low-field MRI. Initially, imaging of flow was demonstrated with a remote detection scheme [74]. Then, Savukov *et al.* showed the first ultra-low-field MRI of static samples using atomic magnetometers [75]. Recently, optically detected MRI was used to investigate flow in porous metallic materials to show that ultra-low-field MRI is a unique technique for revealing defects in porous metals [76]. A third alternative technique, using magneto-resistive sensors, has also been successfully demonstrated for ultra-low-field MRI [77].

A major challenge for ultra-low-field MRI has been poor spatial resolution regardless of which detection technique is used. In addition to the low nuclear magnetization in an ultra-low field, another main reason for the poor spatial resolution is the concomitant field effect, which imposes an upper limit on the gradient field [78, 79]. For instance, for a 10 × 10 imaging grid, the maximum gradient field is approximately 5 μT/cm to avoid substantial image distortion. The situation is particularly severe under ambient conditions because the significant heterogeneity of the magnetic field imposes a lower limit on the gradient field. For example, the homogeneity of the ambient magnetic field in a laboratory environment is approximately 0.1-0.2 μT/cm. This value sets a lower limit of approximately 1 μT/cm for the gradient field. Therefore, the appropriate range for the amplitude of the gradient field is small. Consequently, the spatial resolution is constrained. Several methods for image correction have been proposed and have been experimentally implemented [80-82]. However, the spatial resolution for ultra-low-field MRI has not reached sub-millimeter resolution for both of the in-plane axes.

An additional issue that limits the spatial resolution of ultra-low-field MRI is the low detection efficiency of the alternative techniques. For optical detection with atomic magnetometers, the atomic sensor is usually placed near the nuclear spins. The filling factor is not as optimal as that of an inductive coil, which usually encloses the entire sample. Although the innovative idea of using a flux transformer has been successfully demonstrated, this method only has good sensitivity at approximately 100 kHz because it is based on Faraday induction [75, 83]. Thus, this method is not suitable for investigating metallic materials. New configurations are needed to improve the filling factor in

ultralow magnetic fields, and this improvement will eventually also improve the spatial resolution.

Here, we report a zoom-in imaging method that overcomes the concomitant field effect in an ambient magnetic field. Sub-millimeter resolution has been obtained through the clear revelation of a 0.6 mm gap between two flow channels. Detection is achieved with an optical magnetometer. Through the implementation of a gradient solenoid, the filling factor, and hence, the detection efficiency, is significantly improved. The resultant higher signal level enhanced the spatial resolution.

3.2 Experimental section

3.2.1 Zoom-in scheme and translation stage

Figure 3.1a shows the concept of the zoom-in method. Assuming a field of view (FOV) of 10 cm × 10 cm, a 100 × 100 grid is needed to achieve spatial resolution of 1 mm × 1 mm (Fig. 3.1a, left). Such a large number of encoding steps will most likely make the maximum gradient field comparable to or larger than the ambient field, giving that the gradient field has a lower limit determined by the field in homogeneity. Therefore, the concomitant field effect will be severe. In other words, it is difficult to obtain 1 mm × 1 mm resolution. However, we can instead focus on one (or a few) region(s) of interest by initially imaging a 10 × 10 grid. The significantly reduced number of steps will not cause the concomitant field effect. Then, the center of the gradient stack is moved to the region of interest. A second 10 × 10 image on the reduced field of view is

performed (Fig. 3.1a, right). The net result is that for the region of interest, a high resolution of 1 mm × 1 mm is obtained and the concomitant field effect is avoided because of the reduced field of view.

The zoom-in method requires two conditions. One condition is that the gradient stack be mobile. This condition is easily satisfied for ultra-low-field MRI because the gradient coils are open, lightweight, and use very low current; thus, the coils have high mobility. Fig. 3.1b shows the gradient stack mounted on a two-dimensional translation stage. The magnet that the magnetic field B_0 be large, so that there is room to move the gradient coils to obtain different FOVs and so that the movement is not physically restricts the other requirement. This requirement is easily met by the ambient magnetic field produced by the Earth. An optical atomic magnetometer is used to detect nuclear magnetization with a remote detection scheme (Fig. 3.1c). Here, pre-polarization is achieved with a 2-T permanent magnet. Spatial encoding is performed in the ambient magnetic field. The encoded nuclear spins in water flow inside the detection region, which is inside a multilayer magnetic shield where an atomic sensor resides. The sensitivity of the atomic magnetometer is approximately 80 $fT/(Hz)^{1/2}$.

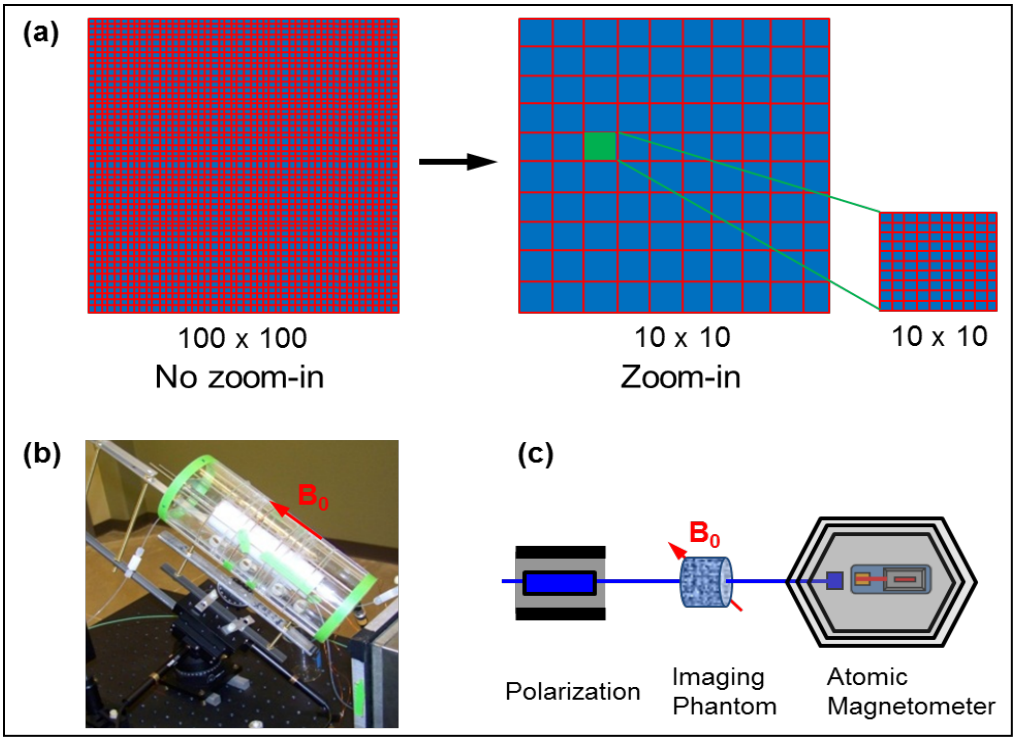

Figure 3.1: Experimental details. (a) Schematic of the zoom-in method. The left panel shows the ordinary imaging method with no zoom-in. The right panel shows the zoom-in method, which consists of two 10 × 10 grids that achieve the same spatial resolution as the ordinary 100 × 100 grid, but only for a region of interest (in green). (b) The coil stack is mounted on a two-dimensional translation stage; the orientation of the coil stack is aligned with the ambient magnetic field B0. (c) Scheme showing the optically detected ultra-low-field MRI of the flow.

The imaging phantom is shown in Fig. 3.2a. The phantom consists of two channels, both 4.0 mm in height but with different widths; one channel is 1.9 mm wide, and the other is 1.6 mm. The gap between the channels is 0.6 mm. The overall length of

the phantom is 10 mm. The translation stages, one for the x-axis and one for the z-axis, have a movement range of 25 mm.

The pulse sequence is similar to the phase encoding sequence used previously (Fig. 3.2b) [74, 76]. The excitation frequency is 2.045 kHz, which corresponds to a magnetic field strength of 48 μT. The duration of the 90º pulse is 6 ms, and the gradient field duration is 5 ms. Phase cycling is used for the second 90º pulse. The field inhomogeneity is measured to be 0.1 μT/cm perpendicular to B_0 (x- and y-axes) and 0.2 μT/cm along B_0 (z-axis). The gradient strength $\Delta G_{x,y}$ was 3.5 μT/cm for the first step of the zoom-in process. For the second encoding step, after moving the gradient stack, ΔG_x was 7.0 μT/cm. ΔG_y was either 3.5 μT/cm.

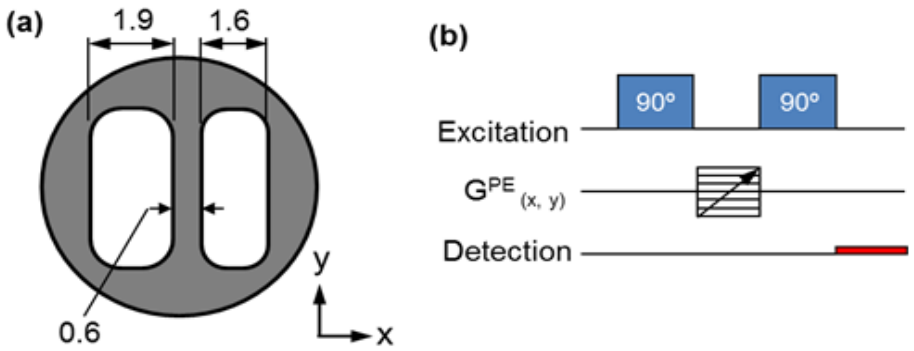

Figure 3.2: Imaging phantom and pulse sequence. (a) Drawing of the phantom with two flow channels spaced by 0.6 mm edge to edge. The units are mm. (b) Pulse sequence. GPE(x, y) is the phase-encoding gradient field along the x- and y-axes. The atomic magnetometer measures the magnetization downstream, as indicated by the red line.

3.2.2 Gradient solenoid

A gradient solenoid was used to guide the nuclear spins while the spins flowed into the detection region inside the magnetic shield (Fig. 3.3). The winding was tight at the left side, which was placed in the ambient magnetic field, and gradually widened toward the right end, which was placed inside the magnetic shield. A dc power supply was used to deliver a constant current to the solenoid. The current was adjusted to maximize the signal. The diameter of the solenoid was 6.5 mm, and the length was 14 cm. The solenoid was hollow so water could flow from the encoding region to the vicinity of the atomic sensor for measurement.

Figure 3.3: The gradient solenoid used to improve the detection efficiency.

3.3 Results and Discussion

3.3.1 Spatial resolution

Fig. 3.4 shows the MR images of water flowing through the phantom at the time of the maximum signal. In Fig. 3.4a, an 11 × 11 grid was used and the FOV was 13 mm × 13

mm. Therefore, the spatial resolution was 1.2 mm × 1.2 mm. Clearly, this resolution was unable to reveal the gap between the two channels. The maximum field produced by the gradient coil at the edge of the FOV was already 12 μT, which was comparable to the B_0 field of 48 μT. Therefore, simply increasing the gradient field to attain higher resolution would cause the concomitant field effect.

The image in Fig. 3.4a showed that the region of interest is approximately 2 mm (indicated by d on the image) from the center of the FOV. Thus, we then moved the gradient stack to the left by 2 mm to magnify the region of interest. The gradient field ΔG_x was doubled to 7.0 μT/cm while ΔG_y remained 3.5 μT/cm. Therefore, the spatial resolution along the x-axis was doubled to 0.6 mm. The resulting image is shown in Fig. 3.4b. The finer spatial resolution was able to resolve two channels; this resolution was lacking in the previous image.

The concomitant field effect was avoided through the simultaneous increase in the gradient strength and reduction in the FOV. The parameter that measures the concomitant field effect is given by $\varepsilon = GL/B_0$, where G is the gradient magnetic field, L is the dimension of the FOV, and B_0 is the leading magnetic field [82]. Based on this equation, the zoom-in method keeps ε constant through a simultaneous increase in the gradient and a decrease in the size of the FOV. However, the spatial resolution is improved. In addition, the new FOV is adjusted to the region of interest. This adjustment is important because without the spatial mobility, the region of interest, indicated by a green box in Fig. 3.4a, would be partially outside of the reduced FOV.

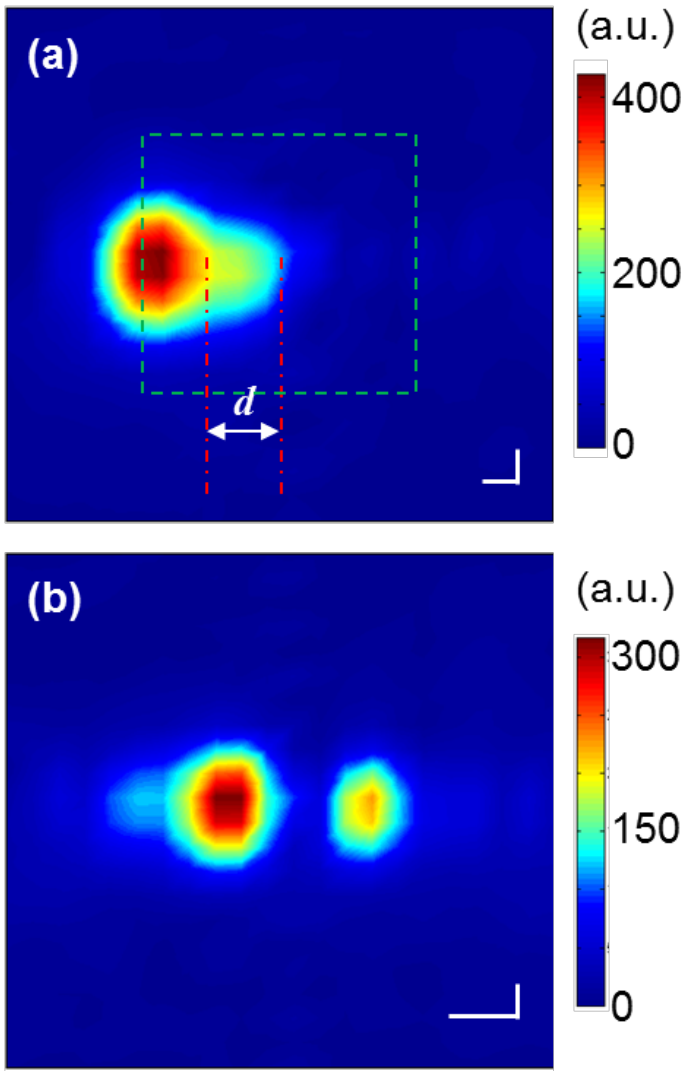

Figure 3.4: Results of using the zoom-in method for ultra-low-field MRI in an ambient magnetic field. (a) MR image before zoom-in. The green box indicates half of the FOV. (b) Zoom-in MR image after the coil stack was moved to the left by 2 mm and the gradient field on the horizontal axis was doubled. The scale bars indicate 1 mm.

Figure 3.5 shows the image with a reduced FOV along both the x- and y-axis by a factor of 2. Therefore, the spatial resolution was 0.6 mm × 0.6 mm, which is the highest

resolution for ultra-low-field MRI to date. The black traces on the image show the actual sizes of the flow channels; these sizes match the MR image well. The connection between the two channels possibly arises from the reduced signal-to-noise ratio of the image or from the area at the ends of the two channels where the channels connect. Note that the amplitude of the signal is substantially lower than that of the images in Fig. 3.4 because of the reduced pixel size.

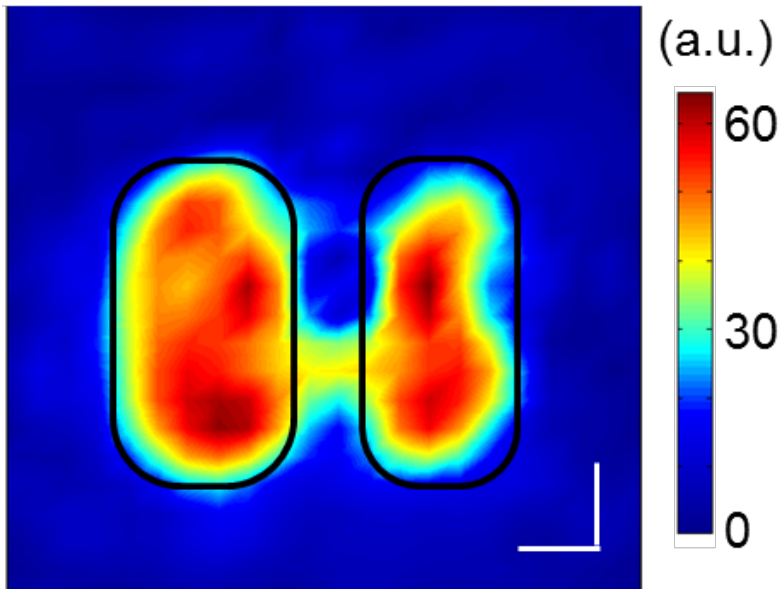

Figure 3.5: Zoom-in MR image acquired by doubling the gradient field along both axes. The scale bars indicate 1 mm.

The zoom-in method not only improves the spatial resolution for ultra-low-field MRI, it also significantly reduces the experimental time required to image continuous flow. This reduction is because the total number of encoding steps is substantially lower with the

zoom-in method. For example, a 100 × 100 grid requires 10^4 encoding steps with pure phase encoding whereas two 10 × 10 grids only require 200 encoding steps. Even if there are five regions of interest, the total imaging time is still reduced 10-fold. The reduction in the number of steps is significant in ultra-low-field MRI because pre-polarization, which usually takes a few seconds for each step, is the speed-limiting process.

A clear disadvantage of the zoom-in method is that it does not provide a high-resolution image of the entire FOV. However, this entire high-resolution image may not be necessary for many applications, where localized images will suffice instead. For example, the identification of clogged regions in a metallic substrate does not require high resolution over the entire FOV [76]. Additionally, medical imaging for diseases often focuses on localized regions with abnormalities. In these cases, our zoom-in method provides a practical approach to high-resolution ultra-low-field MRI.

In addition to using the zoom-in method, we attempted to improve the spatial resolution by increasing the signal amplitude. In optical detection, a guiding magnetic field is essential to allow the nuclear spins to pass through the multi-layer magnetic shield [74, 84]. The guiding field cannot interfere with the near-zero magnetic field needed for the atomic magnetometer in our detection scheme. Previously, a long piercing solenoid was used for the nuclear spins and the atomic magnetometer was placed outside of the middle of the solenoid. This configuration ensures that the atomic sensor does not experience the magnetic field produced by the solenoid. However, this geometry increases the distance between the sample and the atomic sensor. An alternative approach used a pulsed magnetic field to transport the nuclear spins, and this pulsed field was

turned off during the measurement [85]. This approach is not suitable for the imaging of a continuous flow.

3.3.2 Sensitivity

The gradient solenoid shown in Fig. 3.3 provided a magnetic field that gradually decreased from the outside of the magnetic shield to the atomic sensor inside the magnetic shield. The magnetic field of the gradient solenoid bridged the ambient magnetic field outside of the magnetic shield (48 μT) and the near-zero magnetic field where the atomic sensor resided (~0.2 μT). In practice, a current of 0.1 A was used for the solenoid. The magnetic field generated by the last two loops on the solenoid at the atomic sensor position was estimated to be approximately 3 nT. Such a small field would not affect the sensitivity of the magnetometer. Figure 3.6a shows the two magneto optical resonance profiles with and without current in the solenoid. It can be observed that the resonance feature was not broadened after current was supplied to the solenoid. The 7 Hz frequency shift in Fig. 3.6a indicates that a magnetic field of 1 nT was produced by the solenoid; this value is consistent with the estimate of 3 nT. The lower value is most likely because of the shielding of the innermost layer of the magnetic shield.

Figure 3.6b shows the nuclear magnetization measurement for flowing water. A single 180° pulse was applied to invert the spins in the ambient magnetic field. Time zero was set to be the beginning of the pulse. The high amplitude shows that the gradient solenoid effectively guides the nuclear spins that are transported from the ambient

magnetic field to the near-zero field. Compared to previous results with a piercing solenoid [76], the signal was nearly twice as high. Such an increase is substantial given the usually low signal for ultra-low-field MRI.

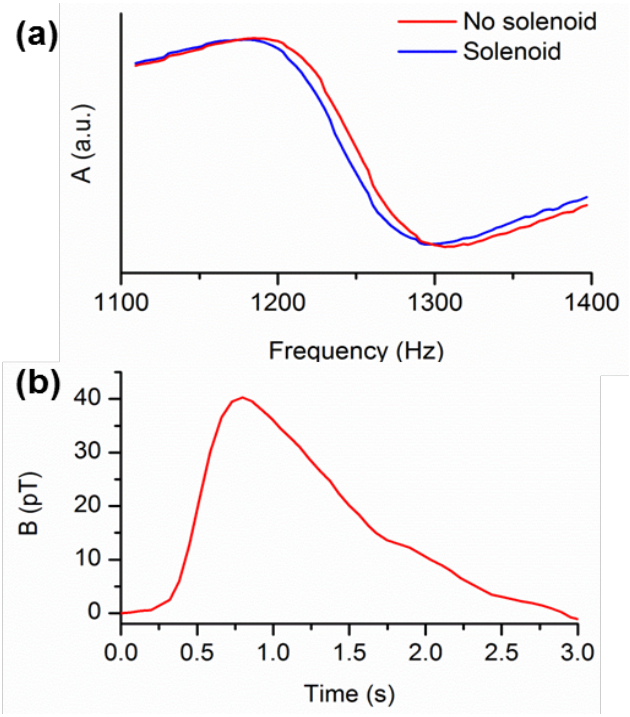

Figure 3.6: Improvement of the detection efficiency with a gradient solenoid. (a) Magneto-optical resonance profiles with and without the gradient solenoid. (b) Water flow profile measured by the atomic magnetometer with a gradient solenoid.

The increase in the signal amplitude can be explained by the improvement in the filling factor. Figure 3.7 shows the schematics of the two different configurations. Based on the geometry, the distance between the sample and the atomic sensor was significantly

shorter when the gradient solenoid was used. The reduction factor was about 1.25, from 10 mm to 8 mm approximately. Because of the r^{-3} dependence of magnetic field, where r is the distance between the sample and the sensor, the signal should increase by nearly a factor of 2. This prediction is consistent with the experimentally measured signal improvement. The increase in the signal facilitates the improvement in spatial resolution through the zoom-in scheme. This facilitation occurs because when the spatial resolution increases, the smaller voxel size contains fewer nuclear spins. The higher detection efficiency helps improve the quality of the images.

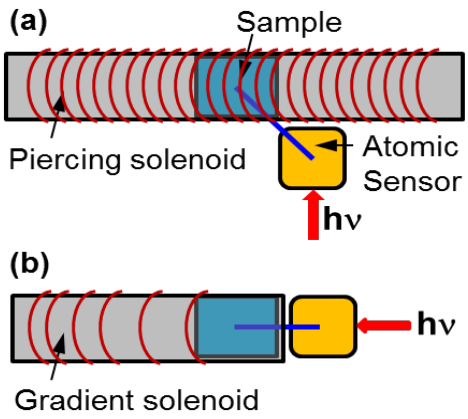

Figure 3.7: Comparison of the filling factors for (a) a piercing solenoid and (b) a gradient solenoid. The blue bars indicate the average distances between the sample and the atomic sensor. The detection axis is determined by the indicated propagation direction of the laser.

Although the idea of a gradient solenoid is specifically useful for the imaging sequence shown here, the zoom-in method is generally applicable for ultra-low-field MRI, whether optical detection is used or not. The method avoids the concomitant field effect, and sub-millimeter resolution can be achieved in the ambient magnetic field. However, the resolution is ultimately limited by the sensitivity of the detection technique and the filling factor. These limits require further development of the detection techniques.

It remains difficult for ultra-low-field MRI to compete with high-field MRI under situations where both are applicable. Nevertheless, ultra-low-field MRI has not nearly reached its limit. For example, recent work by Romalis and coworkers has demonstrated a sensitivity of 0.16 $fT/(Hz)^{1/2}$ [86]. Kitching and colleagues significantly improved the sensitivity of miniaturized atomic sensors [87]. Such high sensitivities have not been used for MRI. Through the coupling of sensitivity, improvements and the new methods developed here, optically detected ultra-low-field MRI can find a wide range of applications. The technique will be particularly valuable in situations where high-field MRI is not applicable, including samples with high magnetic heterogeneity, systems involving metallic materials, and scenarios that require portability.

Chapter 4

4. Ultra-low-field MRI towards generating molecule specific contrast

4.1 Basic concepts in contrast MRI

MRI is considered as one of the most important non-invasive imaging techniques in clinical diagnostics and research. The ability to image tissues with high resolutions in three dimensions has made MRI the best among its counterparts. In the clinical field, the resolution obtained is up to 1 mm and in the research sector, it is even down to about 50 μm at high fields. The unique feature of MRI is the ability to obtain information both on anatomy and on a wide range of physiological parameters within a single examination.

MRI images depend on the RF signals arising from the magnetic moments of tissues containing water protons [88]. The advantages of using water protons as the probe molecule were that protons have highest sensitivity among the biologically relevant nuclei. Proton spin density and longitudinal (T_1) and transverse (T_2) relaxation times play an important role in the normal contrast of the MR images. In some of the soft, considerably healthy tissues, the differences in the relaxation times are sufficient enough to provide inter organ contrast in T_1 weighted and T_2 weighted images. The difference between the pathological tissue and healthy tissue can be made based on the intrinsic

differences in $T_1$and T_2 contrast. However, there are many pathological conditions which do not lead to significant morphological changes. Images from such tissues do not display specific enough changes in the relaxation times. Under these conditions, the pathology may be detected by using MRI contrast agents, which changes the local relaxation times of the diseased tissue. The use of contrast agents has many considerable benefits despite it violates the non-invasive character of MRI technique. The imaging of inflamed tissues like in arthritis [89], tumor angiogenesis [90], atherosclerotic plaques [91], and multiple sclerosis [92] can be greatly enhanced by the combination of MRI and contrast agents.

In recent years, the development in the field of molecular imaging has increased the search for new and more efficient contrast agents. The effort to visualize molecular and cellular processes non-invasively in vivo can be achieved by directing a detectable reporter called nuclear tracer or MRI contrast agent, towards the target molecules or processes of interest. Cell surface receptors, enzyme activity or gene expression and physiological processes were some of the targets of these contrast agents. Positron emission tomography (PET), single photon emission tomography (SPECT) was the nuclear methods in which molecular imaging was the main domain. The main drawbacks of the molecular imaging technique are low spatial resolution and the poor characterization of anatomy. On the other hand, MRI with its good spatial resolution has become a striking alternative. In MRI the problem with the sensitivity has to be taken care of. This can be served by using contrast agents with a high relaxivity. There are five different types of contrast agents available at present.

(i) Non-specific contrast agents

a. Low molecular weight contrast agents.

— e.g.: Gadolinium DTPA

b. High molecular weight blood pool agents.

— e. g.: High generation dendrimers and paramagnetic liposomes.

(ii) Targeted contrast agents

— These contrast agents uses ligands and are actively directed towards specific molecular target.

(iii)Contrast agents for functional imaging

— e. g.: Paramagnetic Mn^{2+}.

(iv)Activated or responsive contrast agents

— These contrast agents change their physical environment because of change in the biological process.

(v) Contrast agents used to label and track cells in living body [93].

MRI uses the imbalance of the spin-up and spin-down protons in a strong magnetic field. The population difference produces a very tiny magnetization in thermal equilibrium. By exciting the protons with radio frequency (RF) field, the equilibrium can be distributed and leaves the system in excited state. The relaxation occurs after turning off the RF field. The two types of relaxation processes are spin-lattice or longitudinal relaxation (T_1) and spin-spin relaxation or transverse relaxation (T_2). The contrast agents act by changing the relaxation times of water protons surrounding the contrast agent. The potency of the contrast agent is defined by the change in the T_1 or T_2 rates per unit concentration of

contrast agent [94]. The proportionality constant, which is expressed in $mM^{-1}s^{-1}$ is called the relaxivity, r_1 or r_2. Relaxivities generally depend on magnetic field strength. To gain knowledge on the relaxation behavior of a specific agent, it is required to record the r_1 and r_2 values as a function of magnetic field strength. Usually r_1 decreases at higher field strength and r_2 stays constant or slightly increases. The contrast agents whether they can be used as T_1 weighted or T_2 weighted can be determined by the ratio of the r_1 and r_2 values. The T_1 contrast agents have a low r_1 over r_2 ratio and so, they can generate images with positive T_1 contrast. On the other hand, T2 contrast agents have a negative contrast on T_2 weighted images, which probably looks like dark spots. A new set of contrast agents called chemical exchange saturation transfer (CEST) agents has been recently proposed [95]. These agents has exchangeable protons and when irradiated at certain specific absorption frequency transfer saturated magnetization to the surrounding water. This transfer of magnetization to the water decreases the water signal intensity and results in dark sports in the images. The contrast generated from these CEST agents can be turned on and off making it possible to detect several agents in the same sample using compounds with different specific absorption frequencies [96].

4.2 Molecule specific contrast imaging

4.2.1 Motivation

Nuclear magnetic resonance (NMR) and magnetic resonance imaging (MRI) techniques distinguish them from other spectroscopic techniques by providing detailed

chemical shift information and contrast for different environment. When NMR/MRI is performed in an ultralow magnetic field (ambient field or below), however, it is challenging to maintain these advantages. This is because chemical shift usually becomes irresolvable. Alternatively, Ledbetter *et al*. reported zero-field J-coupling spectra of a variety of isotope-enriched chemicals [97]. Characteristic J-coupling parameters can provide rich information that will aid determining specific chemicals. Appelt *et al*. measured high-precision J-coupling constants in the Earth's magnetic field using inductive detection [61]. The results contain rich chemical information, but are limited to NMR spectroscopy not imaging.

For contrast imaging, although the contrast based on spin-lattice relaxation (T_1 relaxation) is enhanced in ultra-low-field, no study has reported molecule-specific contrast [98]. For example, Lee and co-workers showed contrast using agarose at a concentration of 2.5% can be observed in 100 μT field, detected by a superconducting quantum interference device (SQUID) [99]. Ruangchaithaweesuk *et al*. demonstrated two commonly used gadolinium chelates have enhanced contrast in the ambient field compared to in high field [100]. Both cases only provide contrast of homogeneous samples, not molecular information in a heterogeneous environment.

Another type of contrast agent, magnetic particles, has also been extensively used in producing contrast MR images. Magnetic particles of micrometer or nanometer sizes reduce both spin-lattice relaxation time (T_1) and spin-spin relaxation time (T_2). Because of the more substantial effect on the latter, magnetic particles are usually categorized as T_2 contrast agent. The versatile surface functionalization for the magnetic particles also

allows their employment in molecular imaging. For instance, antibody-coated magnetic particles will specifically bind to the corresponding antigen molecules. A magnetic device, such as an atomic magnetometer, SQUID, or giant magnetoresistive (GMR) sensor, can directly measure these particles. Usually, the spatial resolution is poor due to the inverse problem in magnetic sensing. One exception is that when the locations of the magnetic particles are finite, their spatial resolution can be precisely obtained by using a scanning magnetic imaging method. For general cases, the conjugated magnetic particles can in principle be detected by ultra-low-field MRI, similar to conventional MRI, based on the negative contrast they induce. However, it is not easy to quantify, and no contrast imaging has been performed in ultra-low-field.

Here we show that molecule-specific contrast can be achieved in ultra-low-field MRI. Using an atomic magnetometer for detection, contrast produced by ligand-conjugated magnetic particles can be distinguished when they bind to the target molecules. The total number of the magnetic particles can be obtained by using the magnetometer to directly measure the magnetic field signal. Combining molecular specificity and spatial information should enable our method to be used for probing surfaces under opaque conditions.

4.2.2 Applications of magnetic particles in molecule sensing and contrast imaging

Iron oxide in the form of Fe_3O_4 has high biocompatibility and low toxicity in human body, which is why it has been widely used in biomedical applications. Functionalized magnetic particles have been associated with drug delivery systems to a

desired target receptor for medication [101, 102]. These nanoparticles are also functionalized with drugs, proteins, and genetic materials and apparently serve as therapeutic agents [101, 103]. The major application for the magnetic nanoparticles is the in-vitro bioassays [105,104]. Ferromagnetic sensors were used to detect binding of DNA and proteins, which results in extremely sensitive magnetic microarrays.

Superparamagnetic iron oxide (SPION) has been used as in vivo MRI contrast agents for molecular and cellular imaging [105, 106]. A polysaccharide layer present on the surface of SPION particles contributes to the colloidal stability [105]. These functionalized particles have been used in a wide variety of applications such as cell separation, protein purification, food analysis, organic and biochemical synthesis, and industrial water treatment [107]. Organic polymers can enhance the stability, dispersability and functionality of the magnetic nanoparticles. The use of iron oxide particles in cancer therapy is another potential application. The study is called hyperthermia where tumor cells can be heated to 41 to 45 °C, from which the cancerous tissues are irreversibly damaged while causing a reversible damage to the normal tissues [101].

The concept of molecule-specific contrast imaging can also be extended for applications in the antigen-antibody interactions and DNA interactions. The binding strength of the antigen-antibody can be estimated by labeling the molecules with magnetic particles. The contrast in the images with respect to the type of force applied can give us information about the specific binding and bond strength. It is the same case with two different strands of DNA. The information about the binding strength between

two different strands of DNA with different combination of base pairs is molecule specific and is possible with the described molecule specific contrast using ultra-low-field MRI.

4.2.3 Biotin-streptavidin linkage

Streptavidin is a tetrameric proteinisolated from the action bacterium Streptomycesa vidinhi (1). Streptavidin, and the homologous protein avidin, are remarkable for their ability to bind up to four molecules of d-biotin with unusually high affinity [dissociation constant $K_d = 10^{-15}M$ [108, 109]].The ability of Streptavidin and avidin to bind derivatized forms of biotin has led the wide spread use of these components in diagnostic assays that require formation of an essentially irreversible and specific linkage between biological macro-molecules [110].

Streptavidin subunits were organized as eight-stranded, anti-parallel β sheets. The sheet comprises of coiled polypeptide chains with a staggered pattern of adjacent strand hydrogen bond registration. This structure visualizes like a cyclically hydrogen bonded barrel with several hairpin loops. The attachment near the carboxyl terminus is free to form a more extended β sheet. A natural streptavidin tetramer is formed by interdigitating a pair of dimers connected with their dyad axes coincident, and produces a particle with 222-point group symmetry. The stability of the tetramer is offered by extensive van der Waals interactions between the subunit barrel surfaces. The binding of biotin occurs in the pockets at the ends of each of the streptavidinβ barrels [111]. Aromatic or polar

amino acid residues were present at the lining of the pockets. The residual groups are mostly solvent exposed in apo-streptavidin so that several water molecules occupy the biotin-binding site residues. The binding of biotin involves displacement of bound water and formation of multiple interactions between biotin heteroatoms and the binding site. The structure of the streptavidin-biotin complex was solved with the use of symmetry-constrained searches of the complex unit cell with the apo-streptavidin tetramer [112]. The following figures show the representation of the attachment of the streptavidin-coated magnetic nanoparticles with the biotin-coated substrate.

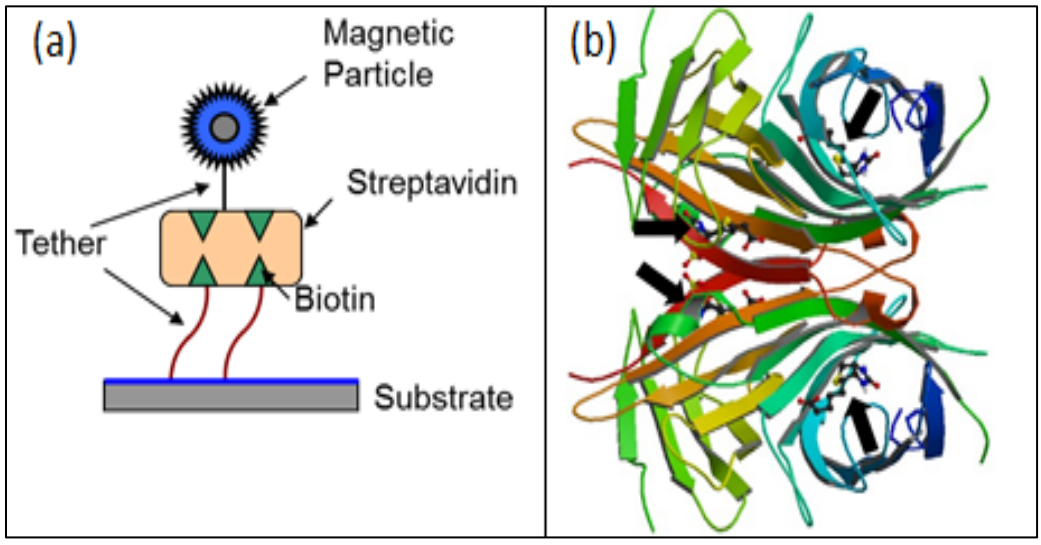

Figure 4.1: (a) The drawing shows the idea of the binding of the streptavidin coated magnetic particle to the biotin substrate. (b) In the picture, four black arrows show the position of the biotin bound to the streptavidin.

4.3 Experimental section

4.3.1 Phantom with streptavidin-coated magnetic particles

Figure 4.2 shows the experimental setup. Contrast imaging was carried out in a phantom divided into two halves. One side of the divider was either coated with biotin for contrast imaging or blank for control. Streptavidin-conjugated magnetic particles are allowed to bind with the biotin surface to form strong and specific streptavidin-biotin bonds. The inset shows the top view of the phantom. Water was pre-polarized by a strong permanent magnet (B_{pp}, 2 T) and then flowed into the phantom to be imaged. The phantom was placed in the ambient mangetic field B_0 and gradient fields $G_{x,y}$. The flow channel in the phantom was 6.5 mm diameter and 10 mm length. After spatial encoding, the water flowed out of the phantom and the signal was measured by an atomic magnetometer. The principle of this remote detection has been described elsewhere.

Streptavidin-coated magnetic particles of two different sizes, 1 μm and 2.8 μm in diameter, have been employed. The 2.8-μm magnetic particles were obtained from Invitrogen, with a number density of approximately 6-7$\times 10^5$ particles/μl. The 1-μm particles were obtained from Chemicell, with a number density of approximately 1.8$\times 10^7$ particles/μl.

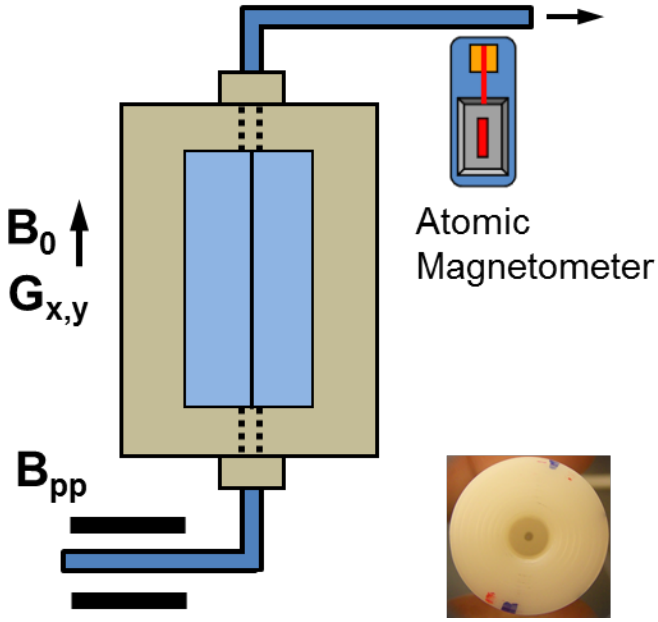

Figure 4.2: Experimental setup. The image phantom is divided into two halves by a piece of glass. Water flows into the phantom after pre-polarization. The encoded water is detected by an atomic magnetometer downstream. Inset shows the top view of the phantom without the dividing glass.

Streptavidin-coated magnetic particles of two different sizes, 1 μm and 2.8 μm in diameter, have been employed. The 2.8-μm magnetic particles were obtained from Invitrogen, with a number density of approximately 6-7×10^5 particles/μl. The 1-μm particles were obtained from Chemicell, with a number density of approximately 1.8×10^7 particles/μl.

The atomic magnetometer used for detection has been reported previously. The sensitivity of the atomic magnetometer is approximately 80 fT/(Hz) $^{1/2}$. A phase-encoding pulse sequence was used for spatial encoding. The excitation frequency was 2.045 kHz,

corresponding to a magnetic field strength of 48 μT. The duration of the π/2 pulse was 6 ms, and the gradient field duration was 5 ms. Phase cycling was used for the second π/2 pulse. The field inhomogeneity was measured to be 0.1 μT/cm perpendicular to B_0 (*x*- and *y*- axes) and 0.2 μT/cm along B_0 (*z*-axis). The gradient strength ΔG_x was 7.0 μT/cm and ΔG_y was 3.5 μT/cm. A gradient solenoid as discussed previously was used to guide the nuclear spins while the spins flowed into the detection region inside the magnetic shield. The flow rate was 27 ml/min.

To quantify the specifically bound magnetic particles, a glass slide coated with biotin was used to be the bottom of a sample well with the dimensions 1×2×4 mm^3 (H×W×L). 1% BSA solution was added to the sample well to minimize non-specific bonding between the magnetic particles and the glass surface. After 1 hr, the BSA solution was replaced with various concentrations of 1.0-μm magnetic particles, diluted using TBS buffer. Incubation time was 90 – 120 min to ensure the binding between streptavidin and biotin molecules. The sample well was then magnetized for 2 min and kept aside for 1 hr for relaxation. During this time, the sample well was subjected to rinsing in a shaker. This was for removing the physisorbed magnetic particles. The magnetic profile of these samples was obtained by scanning the sample across the atomic magnetometer. The magnetic profile of different samples was fitted to obtain the magnetization value.

4.3.2 Instrument setup for selective polarization

For the selective polarization experiment, the two liquids, water and hexane were used. Figure 4.3b shows the experimental setup used for this study. The reservoir tank holds the inlet and the outlet channels. Depending on the density water occupies the bottom layer with hexane on the top. Two separate inlets were employed and operated with two micro pumps. The control for the pump is done by the labview program shown in figures A.1&A.2. The selective polarization is done as we only polarize water by passing it through the permanent magnet. Hexane was not polarized. Polarized water passes throught the side flow and hexane passes through the main flow. By using different flow rate the images were obtained for both the liquids. An optical atomic magnetometer is used to detect nuclear magnetization with a remote detection scheme. Spatial encoding is performed in the ambient magnetic field. The encoded nuclear spins in water flow inside the detection region, which is inside a multilayer magnetic shield where an atomic sensor resides.

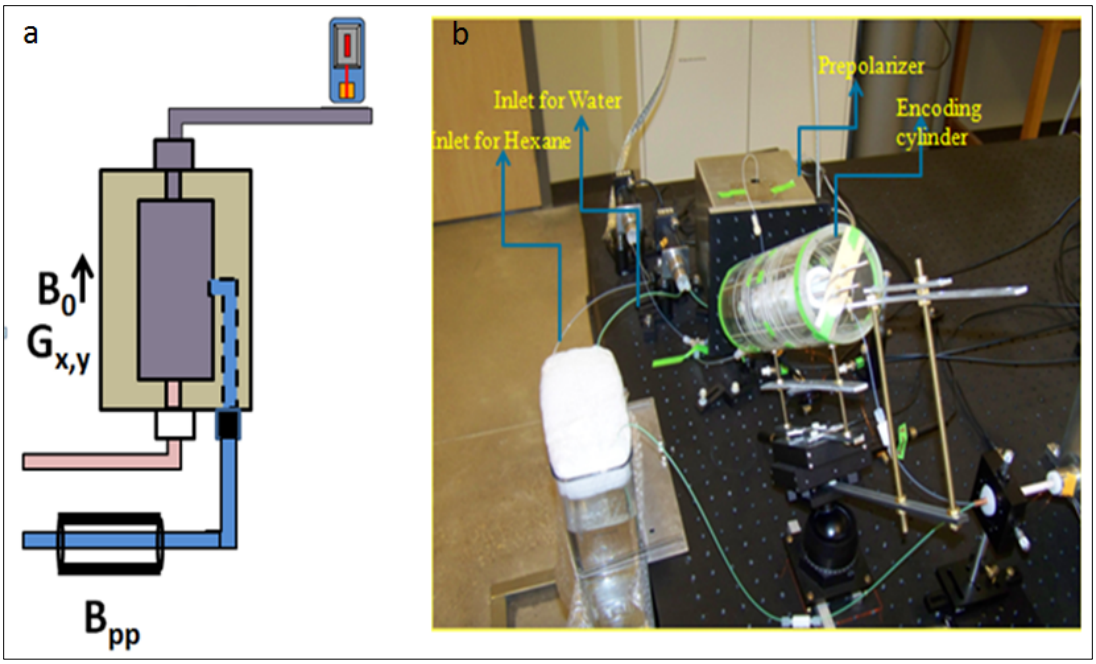

Figure 4.3: (a) Image depicts the setup used for the specific contrast experiment. (b) Photo of the setup for selective polarization showing the inlets for hexane & water. The pre-polarization region and encoding region were also marked.

4.4 Results and discussion

4.4.1 Ligand-conjugated magnetic nanoparticles

Figure 4.4 (a&b) shows the two-dimensional (2D) images with (Figure 4.4a) and without (Figure 4.4b) the presence of 1.0-μm magnetic particles on the surface. The right side in Figure 4.4a has lower intensity compared with the left side, while in the control experiment; the two sides have nearly the same intensities. This confirms the signal loss

in the right side in Figure 4.4a was due to the contrast induced by the magnetic particles. The circles on the images show the diameter of the image phantom. To quantitatively compare the contrast; we obtained the one-dimensional (1D) images on *y*-axis, which is perpendicular to the dividing glass. Figure 4.4 (c&d) also shows the 1D image. Consistent with the 2D images in same figure, the 1D image in the contrast experiment (Figure 4.4c) showed a 10% decrease for the side with magnetic particles, whereas the one in the control experiment showed identical amplitudes (Figure 4.4d). While the 1-μm magnetic particles produced measurable contrast in MR images, the 2.8-μm particles was not able to provide similar effect because they were washed away during the experiment.

Shown in Figure 4.5 are the photos after the dividing glass interacting with the magnetic particles under three different conditions. Figure 4.5a shows the result when no biotin coating was present on the glass. No specific bonds can thus be formed between the magnetic particles and the glass. Not surprisingly, the magnetic particles got washed away by water. When the glass contained biotin coating, it bound the magnetic particles through strong streptavidin-biotin interactions, shown in Figure 4.5b. The magnetic particles remained stable after the experiment. Therefore, the contrast in the MR images shown in Figure 4.4 indicates the existence of biotin molecules on the glass. When the 2.8-μm particles were used, however, the particles disappeared after water flow. This is because the flowing water produced Stokes dragging force, which is proportional with the size of the particles. The photo in Figure 4.5c showed clean glass.

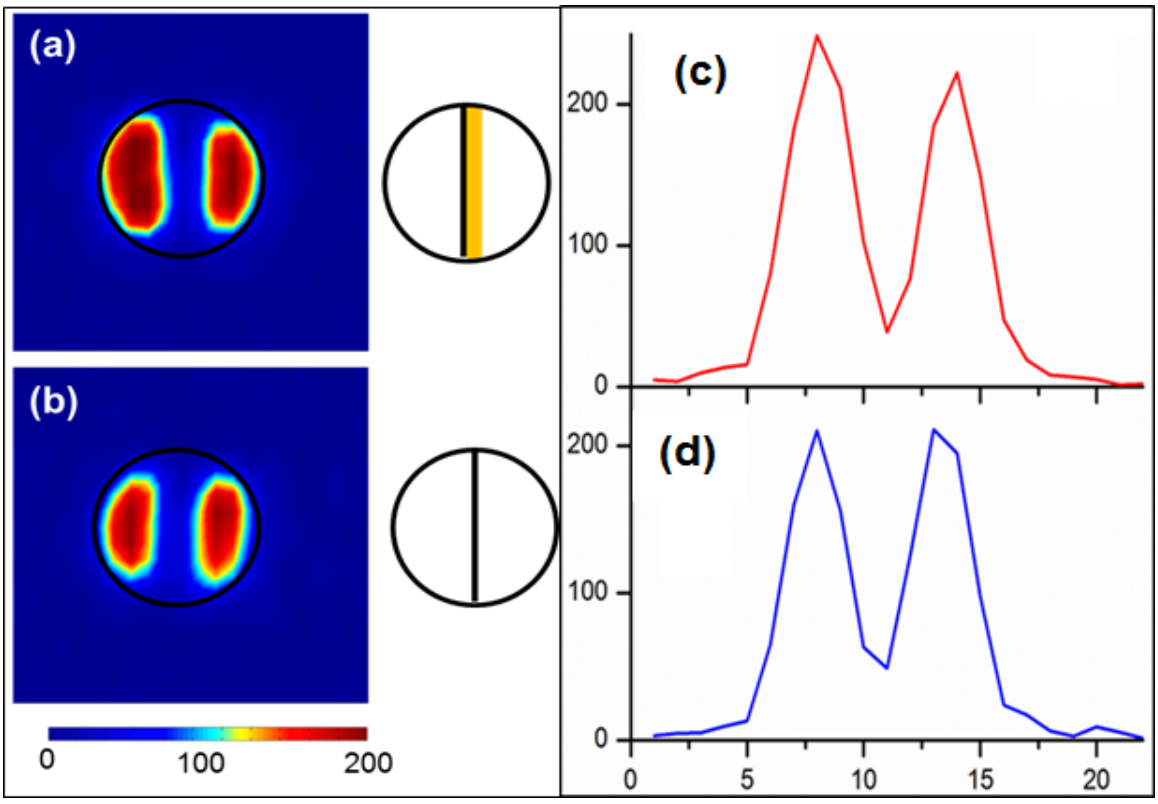

Figure 4.4:Two-dimensional MR images with contrast induced by specifically bound magnetic particles. (a) 2D image of the phantom when the biotin surface was bound with streptavidin-conjugated magnetic particles. (b) Control experiment where the magnetic particles were absent. The cartoons on the right side of each panel schematically show the respective conditions. (c)One-dimensional images for quantitative comparison. (a) 1D image of the phantom across the y-axis, where water on the right side experiences enhanced relaxation by the streptavidin-coated magnetic particles. (d) 1D image for the control experiment.

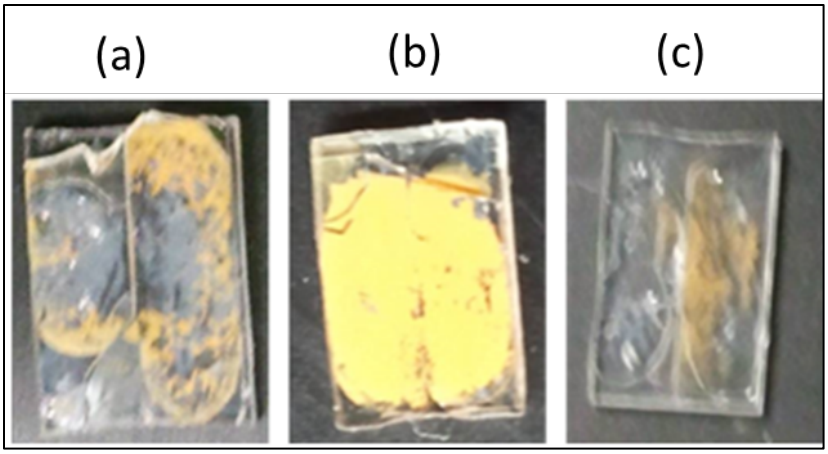

Figure 4.5: Photos of the glass slide after water flowing under three different conditions. (a) Glass without biotin coating interacting with 1-μm particles. (b) Glass with biotin coating interacting with 1-μm particles. (c) Glass with biotin coating interacting with 2.8-μm particles.

The number of the streptavidin-biotin interactions can be quantified by measuring the magnetization of the specifically bound magnetic particles, using the same atomic magnetometer. Figure 4.6a shows the magnetization of the 1-μm particles specifically bound onto the 2×4 mm^2 surface. The magnetization first increased when the quantity of loaded magnetic particles increased. Then the magnetization reached a plateau at 8.3×10^{-10} Am^2, corresponding to approximately 1.7×10^7 particles. This can be interpreted as that the surface with biotin coating is limited. In other words, once the surface is covered completely with the magnetic particles. No more particles can access the biotin molecules on the surface. Therefore a saturation level is reached.

Figure 4.6b shows that the biotin-coated surface was mostly intact after removing the magnetic particles for the probing purpose via contrast MRI. After saturated with magnetic particles, the glass was vigorously washed to remove all the particles from the surface. Then a second batch of magnetic particles was added. The magnetization of the specifically bound particles turned out to be more than 80% of the original value. This indicates that the magnetic particles can serve as probes without damaging the molecule-coated surface. From the saturation study and the dimension of the flow channel in MRI study, we can estimate the detection limit of the molecular interaction. From the surface area of 60 mm^2 for the dividing glass, the total number of specifically bound magnetic particles can be calculated to be 1.3×10^8, or 200 attomole. Such detection limit can make our approach useful for probing a specific type of molecules immobilized on a surface, such as surface of a porous catalyst or a porous medical implant. Under these conditions, optical-based techniques may have difficulty to penetrate the materials.

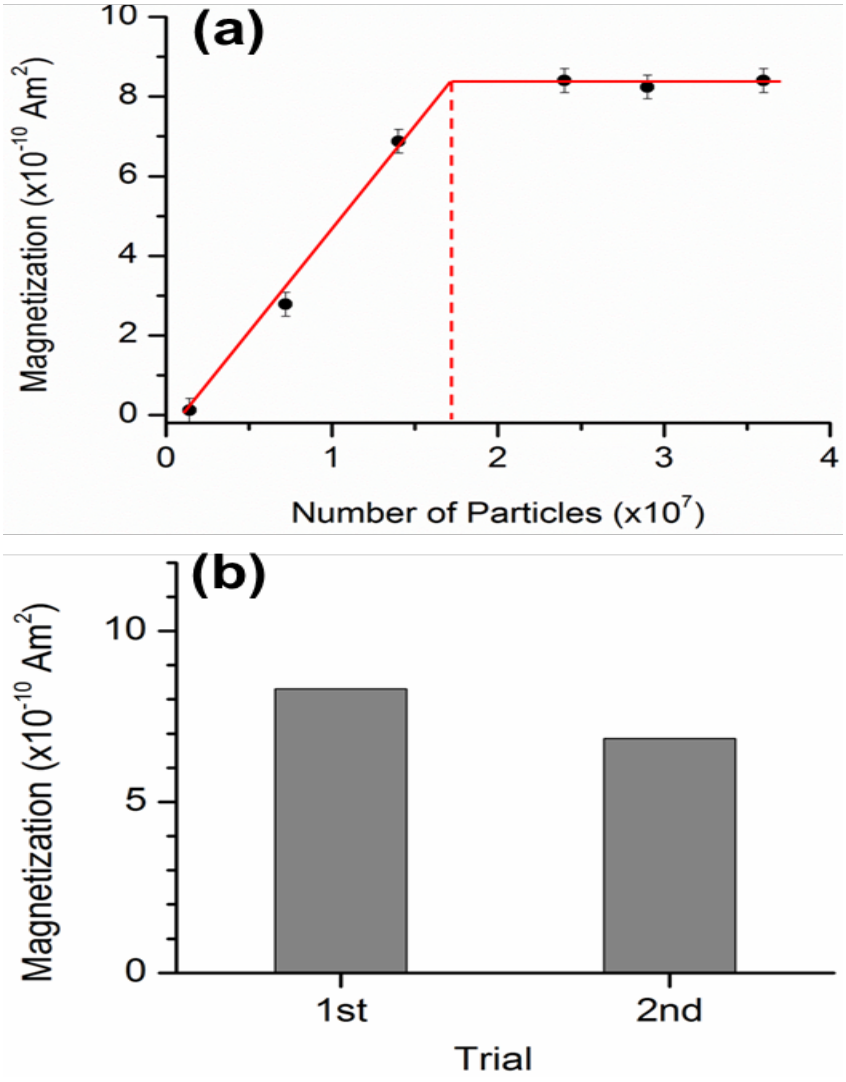

Figure 4.6: Saturation and re-binding studies (a) Magnetization of the 1-μm particles specifically bound onto the 2×4 mm2 surface. (b) The magnetization from both the trials depict the biotin-coated surface was mostly intact after removing the magnetic particles for the probing purpose.

4.4.2 Selective pre-polarization

The experiment was performed at two different speeds. By increasing the tube diameter from 0.02 mm to 0.03 mm the inlet volume of hexane increases from 4.0 ml/min to 18.0 ml/min. Figure 4.8 is the 1D image of the flow system for both the speeds. The magnetization of the high flow rate graph is ~ 30 pT and that of the low flow rate is ~ 28.5 pT. The difference in the magnetization is almost 5 %.

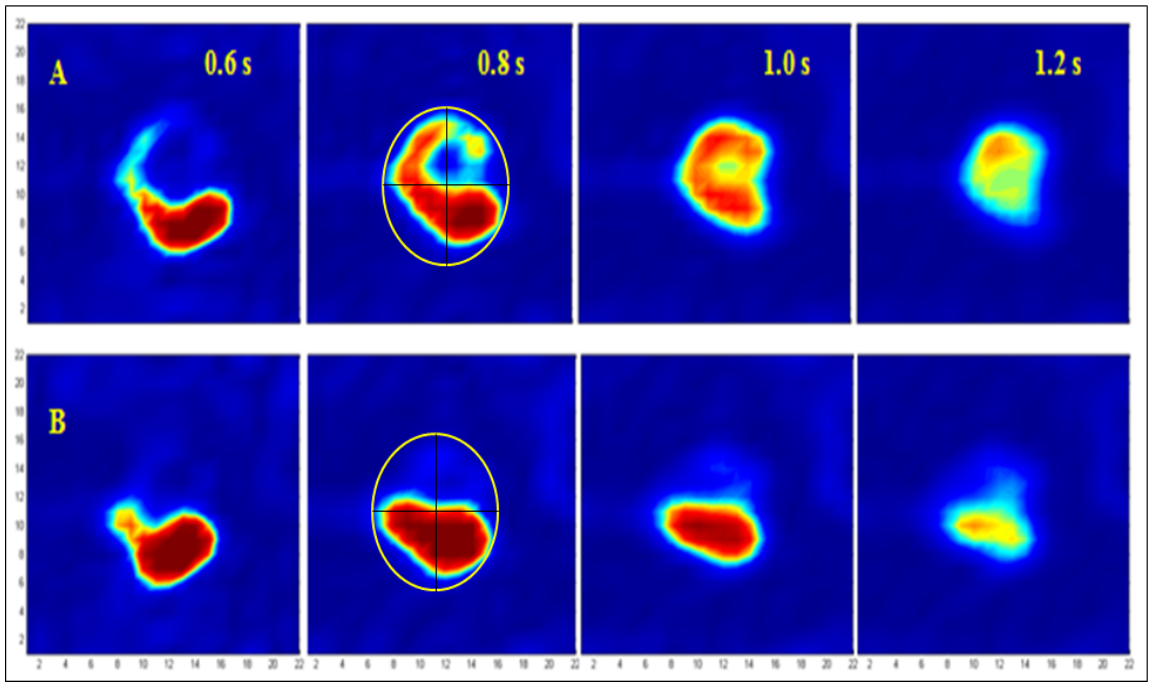

Figure 4.7: 2D image obtained from the specific contrast imaging experiment. A. the 2D image of the sample holder when water and hexane flown in the ratio of 5:1, B. The 2D image of the sample holder when water and hexane flown in the ratio of 1:1.

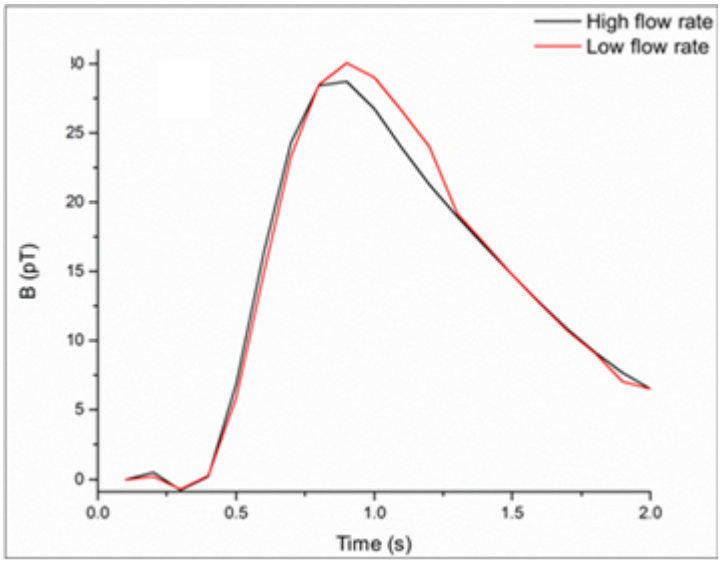

Figure 4.8: The difference in the contrast of the images is clear and is supported by the 1D image in C.

To better understand these observations, we then conducted two-dimensional imaging for the setup. The pulse sequence for phase encoding and the MR images are similar to that of the contrast imaging experiment. The flow direction is along the z-axis, which is the center of the cylindrical sample holder; the x-axis is perpendicular to the z-axis. The 2D image is taken along the xy-axes, which would give the cross-section image of the sample holder. The gradient steps are 18 mG/mm for both the axis. The duration of the gradients is 5 ms. The flow time here is the duration between the first $\pi/2$ pulse and when the encoded water reaches the detection region. In figure 4.7 a & b, the image at 0.8 s has the highest signal and the following discussion refers to the image at 0.8 s. The circle is the space in the sample holder and the lines divide the sample in to four equal quarters. Considering the lower half space in the sample holder, the image in 4.7a has

almost covered 80% and image 4.7b covered > 90% of the available space. However, for the image in 4.7b, there is no signal in the other half of the sample area. The image in 4.7a has water signal in the top left quarter as well. Because of the selective polarization technique, it is made possible to identify the proportions of the liquids inside the holder. The idea of selective polarization is unique for the ultralow field MRI. This pattern of pre-polarization provides many useful applications. For example, the flow dynamics and distribution of the reactants in the labeled channel can be attained before, at some point in, and after it undergoes chemical reactions. In the study done by Ruangchaithaweesuk *et al*. a clogged region in a porous metal was detected using optically detected MRI but not optical imaging or scanning electron microscopy. Based on these recent examples, and with further developments in future, this contrast imaging can be a promising technique to study the details of flow dynamics of liquids with different chemical groups.

Chapter 5

5. Conclusions

In the present thesis work, a zoom-in method to obtain high-resolution images for ultra-low-field MRI is described. The method overcomes the limitation on the gradient field imposed by the concomitant field effect and overcomes the heterogeneity of the ambient magnetic field. A sub-millimeter resolution of 0.6 mm × 0.6 mm has been achieved, demonstrated by the excellent resolution of two channels separated by a 0.6-mm gap. The spatial resolution is also facilitated with a gradient solenoid. We investigated and found that molecule-specific contrast can be achieved by using ligand-conjugated magnetic particles. The detection limit is on the order of 10^8 specific bonds. The size of the magnetic particles cannot be too big, otherwise they will not bind stably with the target molecules under flow conditions. And finally the selective polarization experiment, for the first time with two different liquids was found successful. At different flow speeds, there was a 5% difference in the proton signal. The techniques and results in the present study would contribute to the development of wide range of applications and improvements to the ultra-low-field MRI.

APPENDIX

A.1 LABVIEW for dual pump

In our experiment for the investigation of chemical specificity with selective polarization scheme, we have to control the flow of two different liquids. The idea involved is that both the liquids should come in to contact and mix inside the sample holder. This is made possible by using two micro pumps instead of one. The inlets for the pumps come from the same reservoir. The control for both the pumps is same as for the single pump. We used a 9 pin serial splitter Cable (DB9 1M / 2F RS232) to connect the controls for the two pumps. At a speed of 2100 rpm, with the 0.03 mm diameter tubes, the pump delivered 36 ml of hexane and water (18 ml for each liquid). The Labview program and the block diagram, which controls the pumps, are shown in figures 4.7 and 4.8 respectively.

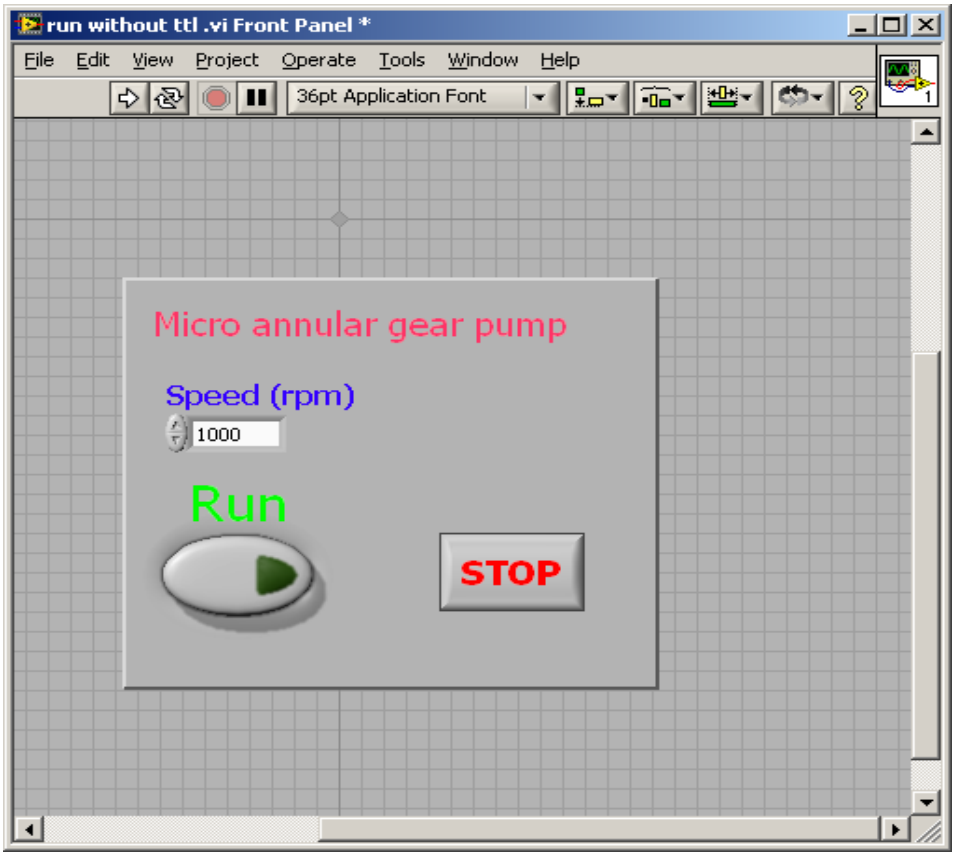

Figure A.1 : Labview program used for operating the pumps

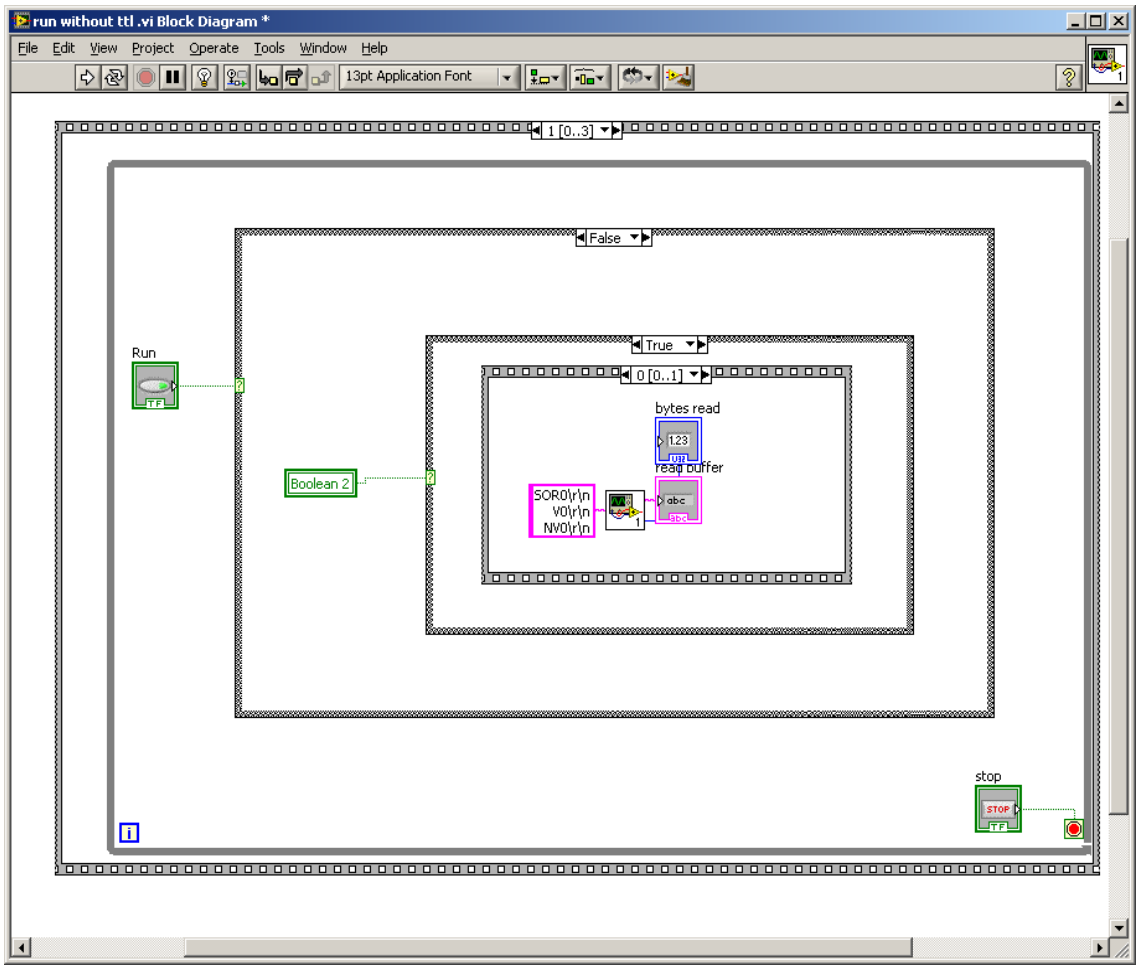

Figure A.2: Block diagram of the Labview program where the speed and other controls can be created and set for operation

A.2 MATLAB script

The MATLAB script used for obtaining the video of the flow profile in a 2d view is given.

```
clear all;
tic
%%%%%%%%%%%%%%%%%%%%%%%%%%%%%%%%%%%%%%%%%%%%%%%%
%%%%%%%%%%%%%%%%%%%%%%%%%%%%%%%%%%%%
% This code is used to generate the 2D MRI image with time flow.
%%%%%%%%%%%%%%%%%%%%%%%%%%%%%%%%%%%%%%%%%%%%%%%%
%%%%%%%%%%%%%%%%%%%%%%%%%%%%%%%%%%%%
% Travel time
period = 0.01;
time_ini = 0.3;
time_final = 1.8;
t_travel = time_ini:period:time_final;
% t_travel = [0.5 0.8];
% Number of steps for a single scan. Change the bottom tool.
% 2D steps from pulse program.
step_1D = 9; % For the signal (column 4), we have x, -x, y, -y phases.
% And for each phase, we take the step (=17) numbers.
% 3D steps from pulse program.
step_2D = 11;
```

```
step = step_1D*step_2D;
size_temp = 30;  % Number of points per flow profile. (average = 1 --> 50, average = 30
--> 30)
% Loop of data
filename = 'lock001a'; % lock005 lock001 (30)
workpath = 'Shoujun\2012 - 2nd half\09202012';
setenv('DYLD_LIBRARY_PATH', '\usr\local\bin\');
output_folder = ['\',workpath]; % All the data files generated will be stored in this folder
path_data = strcat(output_folder,['\',filename]);
% Output pathnames
path_output = strcat(output_folder);
% Save result
out_filename = 'data_2D.mat';
out_path_data = strcat(output_folder,['/',out_filename]);
% out_filename_time = 'result_time_2D.gif';  % Filename of gif file
out_filename_time = 'result_time_2D.avi';  % Filename of gif file
% Load data
rawdata = importdata(path_data);
% Editing the crap bits out of lock, keeping the time,Diffsig,and Trigger
M(:,1) = rawdata(:,1);
M(:,2) = rawdata(:,4);
M(:,3) = rawdata(:,5);
```

```
clearrawdata
% Finds the first point of a given trigger. Slicing data up into 8 point sections.
% hu means the starting point of each trigger.
trigger_threshold = 3;
hu = [];
for n = 2:length(M);
if (M(n,3)<trigger_threshold)&&(M(n-1,3)>trigger_threshold)
hu = [hu n];
end
end
% Check the missing data
error = find(diff(hu)>79)+1;  % 79 is a threshold. It can be modified.
error2 = find(diff(hu)>79)+1;
ifisempty(error)==0
time = M(:,1)';
haha = (time(hu(error))+time(hu(error2)))/2;
disp('Some data are missing. The positions are at')
num2str(haha-0.1)
break
end
% Data analysis
tri_back = 6;     % For each trigger, we take 6 points. --> Then, signal.
```

```
aaa_time = [];
peakadd = MRI_analyze(hu,M,step,size_temp,t_travel,tri_back);
a1 = peakadd(:,1);
a2 = peakadd(:,2);
a3 = peakadd(:,3);
a4 = peakadd(:,4);
real_temp = (a1-a2)/2;
imag_temp = (a3-a4)/2;
total = real_temp + 1i*imag_temp;
for mm = 1:length(t_travel)
total_temp = total((mm-1)*step+1:mm*step);
total_temp = reshape(total_temp,step_1D,step_2D);
b = fftshift(fftshift(fft(fft(total_temp,2*step_1D,1),2*step_2D,2),1),2); % Don't forget to
adjust the first number!?!
aaa_time(:,:,mm) = abs(b);
save(out_path_data,'aaa_time')
end
toc
% Preallocate movie structure.
mov(1:length(t_travel)) = struct('cdata', [],...
'colormap', []);
% Plot figure (time flow)
```

```
figure(1);
set(gca,'fontsize',24)
forkk = 1:length(t_travel)
pcolor(aaa_time(:,:,kk));
time = time_ini + period*(kk-1);
title(['Time = ',num2str(time),' sec'])
xlabel('Pixel')
ylabel('Pixel')
caxis([min(min(min(aaa_time))) max(max(max(aaa_time)))])
%    caxis([0  128.5272])
shadinginterp;
set(gcf,'Renderer','painters');
pause(0.1)
mov(kk) = getframe(gcf);
%    % Save above figure as a gif file
%    f = getframe(gcf); % Capture screen shot
%    imind = frame2im(f);
%    [imind,cm] = rgb2ind(imind,256);
%    if kk == 1
%       imwrite(imind,cm,out_filename_time,'gif', 'Loopcount',inf,'DelayTime',0.1);
%    else
%       imwrite(imind,cm,out_filename_time,'gif','WriteMode','append','DelayTime',0.1);
```

```
%    end
end
% movefile(out_filename_time,output_folder) % Move the file to the indicated folder
movie2avi(mov,out_filename_time, 'compression', 'None');
movefile(out_filename_time,output_folder) % Move the file to the indicated folder
```

References

[1] F. Bloch, W, Hansen, M. Packard. *Physical Review*. **1946**, *69*, 127-127.

[2] E. Purcell, H. Torrey, R. Pound. *Physical Review*. **1946**, *69*, 37-38.

[3] P.C. Lauterbur. *Nature*. **1973**, *242*, 190-191.

[4] P. Mansfield, P. K. Grannell. *Journal of Physics C: Solid State Physics*. **1973**, *6*, L422-L426.

[5] P. Mansfield, A. M. Blamire, R. Coxon, P. Gibbs, D. N. Guilfoyle, P. Harvey, M. Symms, J. C. Waterton, P. A. Bottomley, A. N. Garroway, G. K. Radda. *Philosophical Transactions: Physical Sciences and Engineering*. **1990**, *333*, 495 - 506.

[6] H. Pearson. *Nature*. **2003**, *425 (6958)*, 547-547.

[7] M. Mantle. *Progress in Nuclear Magnetic Resonance Spectroscopy*. **2003**, *43*, 3-60.

[8] B. Blumich. NMR imaging of materials. *Oxford: Claredon Press*; **2000**.

[9] M. Mößle, S. I. Han, W. R. Myers, S. Lee, N. Kelso, M. Hatridge, A. Pines, J. Clarke. *Journal of Magnetic Resonance*. **2006**, *179*, 146-151.

[10] E. Harel, L. Schroder, S. Xu. *Annual Review of Analytical Chemistry*. **2008**, *1*, 133-163.

[11] M. Möβle, S.-I. Han, W.R. Myers, S.K. Lee, N. Kelso, M. Hatridge, A. Pines, J. Clarke, *Journal of Magnetic Resonance*. **2006**, *179,* 146-151.

[12] Abragam. The Principles of nuclear magnetism. Clarendon Press, Oxford, UK. **1961**.

[13] E. Purcell, H. Torrey, R, Pound. *Physical Review*. **1946**, *69*, 37-38.

[14] F. Bloch. *Physical Review*.**1946**. *70*, 460–4740.

[15] C. P. Slichter, Principles of magnetic resonance, *Springer-Verlag*, New York, 3rd edition. **1990**

[16] P. A. Bottomley, T. H. Foster, R. E. Argersinger, and L. M. Pfeifer. *Medical physics.* **1984**, *11*, 425–448.

[17] S. E. Ungersma, N. I. Matter, J.W. Hardy, R. D. Venook, A. Macovski, S. M.Conolly, and G. C. Scott. *Journal of Magnetic resonance*.**2006,** *55*, 1362–1371.

[18] S. Hartwig, J. Voigt, H.-J. Scheer, H.-H. Albrecht, M. Burghoff, and L. Trahms. *Journal of Chemical Physics***. 2011**, *135*, 054201.

[19] H. C. Torrey. *Physical Review*. **1956**, *104*, 563–565.

[20] F. Bloch. *Physical Review*. **1946**, *70*, 460–474.

[21] J. Hsieh. Principles, Design, Artifacts, and Recent Advances. SPIE, Bellingham, Washington, USA, 2nd edition. **2009**.

[22] Fenster, D. B. Downey, and H. N. Cardinal. *Physics in Medicine and Biology.* **2001.** *46*, R67–R99.

[23] P. C. Lauterbur. *Nature*. **1973**, *242*, 190–191.

[24] D. K. Sodickson and W. J. Manning. *Magnetic Resonance*. **1997**, *38*, 591–603.

[25] F.-H. Lin, L. L. Wald, S. P. Ahlfors, M. S. Hamalainen, K. K. Kwong, and J. W. Belliveau. Magnetic Resonance. **2006**, *56,* 787–802.

[26] M. Weiger, K. P. Pruessmann, R. Osterbauer, P. Bornert, P. Boesiger, and P. Jezzard. Magnetic Resonance. **2002**, *48*, 860–866.

[27] C. Preibisch, U. Pilatus, J. Bunke, F. Hoogenraad, F. Zanella. *Neuro Image.* **2003,** *19*, 412–421.

[28] P. B. Roemer, W. A. Edelstein, C. E. Hayes, S. P. Souza, and O. M. Mueller. *Magnetic Resonance*. **1990**, *16*, 192–225.

[29] M. Packard and R. Varian. *Physical Review*. **1954**, *93,* 941.

[30] R. McDermott, S. K. Lee, B. ten Haken, A. H. Trabesinger, A. Pines, and J. Clarke. *Proceedings of the National Academy of Sciences.* USA. **2004**, *101*, 7857–7861.

[31] R. McDermott, A. H. Trabesinger, M. Muck, A. Pines, and J. Clarke. *Science.* **2002**, *295*, 2247–2249.

[32] R. McDermott, S. K. Lee, B. ten Haken, A. H. Trabesinger, A. Pines, and J. Clarke. *Proceedings of the National Academy of Sciences.* USA. **2004**, *101*, 7857–7861.

[33] C. H. Tseng, G. P. Wong, V. R. Pomoroy, R. W. Mair, D. P. Hilton, D. Hoffmann, R. E. Stoner, F. W. Hersman, D. G. Cory, and R. L. Walsworth. *Physical Review Letters*. **1998**, *81*, 3785–3788.

[34] M. Mosle, W. R. Myers, S.-K. Lee, N. Kelso, M. Hatridge, A. Pines, and J. Clarke. *IEEE Transactions on Applied Superconductivity.***2005**, *15*, 757–760.

[35] V. S. Zotev, A. N. Matlashov, P. L. Volegov, I. M. Savukov, M. A. Espy, J. C. Mosher, J. J. Gomez, and R. H. Kraus. *Journal of Magnetic Resonance*. **2008**, *194*, 115–120.

[36] P. L. Volegov, A. N. Matlachov, M. A. Espy, J. S. George, and R. H. Kraus, Jr. *Magnetic Resonance*. **2004**, *52*, 467–470.

[37] A. N. Matlachov, P. L. Volegov, M. A. Espy, R. Stolz, L. Fritzsch, V. Zakosarenko, H.-G. Meyer and R. H. Kraus. *IEEE Transactions on Applied Superconductivity*.**2005**, *15*, 676–679.

[38] S. K. Lee, M. Mosle, W. Myers, N. Kelso, A. H. Trabesinger, A. Pines, and J. Clarke. *Magnetic Resonance*. **2005**, *53*, 9–14.

[39] M. Espy, S. Baguisa, D. Dunkerley, P. Magnelind, A. Matlashov, T. Owens, H. Sandin, I. Savukov, L. Schultz, A. Urbaitis, and P. Volegov. *IEEE Transactions on Applied Superconductivity*. **2011**, *21*, 530–533.

[40] J. Clarke, M. Hatridge, M. Mößle. *Annual Review of Biomedical Engineering*. **2007**, *9*, 389-413.

[41] D. Budker and M. Romalis, *Nature Physics*. **2007**, *3*, 227.

[42] H. Weinstock. SQUID sensors: fundamentals, fabrication, and applications.

[43] E. Harel, L. Schroder, S. Xu. *Annual Review of Analytical Chemistry*. **2008**, *1*, 133-163.

[44] I. K. Kominis, T. W. Kornack, J. C. Allred, M. V. Romalis. *Nature*. **2003**, *422*, 596-599.

[45] H. C. Seton, J. M. Hutchison, D. M. Bussell. *Measurement Science and Technology*. **1997**, *8(2),* 116-120.

[46] S. K. Lee, M. Mössle, W. Myers, N. Kelso, A. H. Trabesinger, A. Pines, J. Clarke. *J. Magnetic resonance in medicine. Official Journal of the Society of Magnetic Resonance in Medicine / Society of Magnetic Resonance in Medicine.* **2005**, *53*, 9-14.

[47] E. Harel, L. Schroder, S. Xu. *Annual Review of Analytical Chemistry*. **2008**, *1*, 133-163.

[48] J. Clarke, A. I. Braginski. The SQUID Handbook: Fundamentals and technology of SQUIDS and SQUID systems. *Wiley-VCH*, **2006**

[49] H. Dehmelt. *Physical Review*. **1957**, *105*, 1924-1925.

[50] W. Bell, A. Bloom. *Physical Review*. **1957**, *107*, 1559-1565.

[51] L.W. Parsons, Z. M. Wiatr. *Journal of Scientific Instruments*. **1962**, *39*, 292.

[52] C. Cohen-Tannoudji, J. DuPont-Roc, S. Haroche, F. Laloë. *Physical Review Letters.* **1969**, *22*, 758-760.

[53] Kastler, A. *Journal of Optical Society of America.* **1957**, *47(6)*, 460-465.

[54] I. M. Savukov, S. J. Seltzer, M. V. Romalis. *Journal of Magnetic Resonance.* **2007**, *185*, 214-220.

[55] S. Xu, S. M. Rochester, V. V. Yashchuk, M. H. Donaldson, D. Budker. *Review of Scientific Instruments*. **2006**, *77*, 83106-83108.

[56] M. V. Balabas, D. Budker, J. Kitching, P. D. Schwindt, J. E. Stalnaker. *J. Opt. Soc. Am. B*. **2006**, *23*, 1001-1006.

[57] D. Yu, N. Garcia, S. Xu. *Concepts in Magnetic Resonance Part A.***2009**, *34A*, 124-132.

[58] L. M. Barkov, D. A. Melik-Pashayev, and M. S. Zolotorev. *Optics Communications.* **1989**, *70(6)*, 283-284.

[59] D. Budker, D. F. Kimbll, S. M. Rochester, V. V. Yashchuk, and M. Zolotorev. *Physical Review.* **2000**, *62(4),* 1-7.

[60] W. Gawlik, L. Krzemien, S. Pustelny, D. Sangla, J. Zachorowski, M Graf, A. O. Sushkov, and D. Budker. *Applied Physics Letters*. **2006**, *88(13),* 131108-1-131108-3.

[61] S. Appelt, F. W. Häsing, et al. Chemical Physics Letters. **2007.** *440(4–6),* 308-312.

[62] Finkler, Y. Segev, Y. Myasoedov, M. L. Rappaport, L. Ne'eman, D. Vasyukov, E. Zeldov, M. E. Huber, J. Martin, and A. Yacoby. *Nano Letters.* **2010,** *10*, 1046.

[63] G. Balasubramanian, I. Y. Chan, R. Kolesov, M. Al-Hmoud, J. Tisler, C. Shin, C. Kim, A. Wojcik, P. R. Hemmer, A. Krueger, T. Hanke, A. Leitenstorfer, R. Bratschitsch, F. Jelezko, and J. Wrachtrup. *Nature.* **2008**, *455*, 648-651.

[64] J. R. Maze, P. L. Stanwix, J. S. Hodges, S. Hong, J. M. Taylor, P. Cappellaro, L. Jiang, M. V. G. Dutt, E. Togan, A. S. Zibrov, A. Yacoby, R. L. Walsworth, and M. D. Lukin. *Nature.* **2008**, *455*, 644-647.

[65] G. Balasubramanian, P. Neumann, D. Twitchen, M. Markham, R. Kolesov, N. Mizuochi, J. Isoya, J. Achard, J. Beck, J. Tissler, V. Jacques, P. R. Hemmer, F. Jelezko, and J. Wrachtrup. *Nat Mater.* **2004,** *8*, 383-387.

[66] L. S. Bouchard, E. Bauch, V. M. Acosta, and D. Budker. *New Journal of Physics*. **2011**, *13*, 025017, 1-11.

[67] B. J. Maertz, A. P. Wijnheijmer, G. D. Fuchs, M. E. Nowakowski, and D. D. Awschalom. *Applied Physics Letters*. **2010**, *96*, 092504, 1-3.

[68] S. Steinert, F. Dolde, P. Neumann, A. Aird, B. Naydenov, G. Balasubramanian, F. Jelezko, and J. Wrachtrup. *Review of Scientific Instruments*. **2010,** *81*, 043705, 1-5.

[69] S. K. Lee, M. Möβle, W. R. Myers, N. Kelso, A. H. Trabesinger, A. Pines, J. Clarke. *Magnetic Resonance*. **2005**, *53*, 9-14.

[70] V. S. Zotev, T. Owens, A.N. Matlashov, I. M. Savukov, J. J. Gomez, M. A. Espy. *Journal of Magnetic Resonance*. **2010**, *207*, 78-88.

[71] J. Dabek, P. T. Vesanen, K. C. J. Zevenhoven, J. O. Nieminen, R. Sepponen, R. J. Ilmoniemi. *Journal of Magnetic Resonance*. **2012**, *224*, 22-31.

[72] J. Hatta, M. Miyamoto, Y. Adachi, J. Kawai, G. Uehara. *IEEE Transactions on Applied Superconductivity*. **2011,** *21*, 526-529.

[73] H.-H. Chen, H.-C. Yang, H.-E. Horng, S. H. Liao, S.-Y. Yang, K. L. Chen, L. W. Wang, M. J. Chen. *IEEE Transactions on Applied Superconductivity*. **2011**, *21*, 505-508.

[74] S.-J. Xu. V. V. Yashchuk, M. H. Donaldson, S. M. Rochester, D. Budker, A. Pines, *Proceedings of the National Academy of Sciences*. **2006**, *03*, 12668-12671.

[75] I. M. Savukov, V. S. Zotev, P. L. Volegov, M. A. Espy, A. N. Matlashov, J. Gomez, R. H. Kraus. *Journal of Magnetic Resonance*. **2009**, *199,* 2188-2191.

[76] S. Ruangchaithaweesuk, D. S. Yu, N. C. Garcia, L. Yao, S.-J. Xu. *Journal of Magnetic Resonance.* **2012**, *223*, 20-24.

[77] N. Sergeeva-Chollet, H. Dyvorne, J. Dabek, Q. Herreros, H. Polovy, G. Le Goff, G. Cannies, M. Pannetier-Cecoeur, C. Fermon. *J. Phys. Conf. Ser.* **2011**, *303*, 012055, 1-6.

[78] C. A. Meriles, D. Sakellarious, A. H. Trabesinger, V. Demas, A. Pines. *Proc. Natl. Acad. Sci. USA.* **2005***, 102*, 1840-1842.

[79] P. L. Volegov, J. C. Mosher, M. A. Espy, R. H. Kraus. *Journal of Magnetic Resonance.* **2005**, *175*, 103-113.

[80] W. R. Myers, M. Möβle, J. Clarke. *Journal of Magnetic Resonance*. **2005**, *177*, 274-284.

[81] L.-S. Bouchard. *Physical Reviews*. **2006**, *74*, 054103, 1-11.

[82] J. O. Nieminen, R. J. Ilmoniemi. *Journal of Magnetic Resonance*. **2010**, *207*, 213-219.

[83] I. Savukov, T. Karaulanov, A. Castro, P. Volegov, A. Matlashov, A. Urbatis, J. Gomez, M. Espy. *Journal of Magnetic Resonance*. **2011**, *211*, 101-108.

[84] I. M. Savukov, S. J. Selter, M. V. Romalis. *Journal of Magnetic Resonance.* **2007,** *185*, 227-33.

[85] M. P. Ledbetter, C. W. Crawford, A. Pines, D.E. Wemmer, S. Knappe, J. Kitching, D. Budker. *Journal of Magnetic Resonance*. **2009**, *199*, 25-29.

[86] H. B. Dang, A. C. Maloof, M. V. Romalis. *Applied Physics Letters*. **2010**, *97*, 151110.

[87] V. Shah, S. Knappe, P. D. D. Schwindt, J. Kitching. *Nature Photonics*. **2007**, *1,* 649-652.

[88] E. M. Haacke, R. W. Brown, M. R. Thompson, R. Venkatesan. Magnetic Resonance Imaging, Physical principles and sequence design; *John Wiley & Sons*: Newyork, **1999**.

[89] M. A. Lutz, C. Seemayer, C. Corot, E. R. Gay, K. Goepfret, A. B. Michel, B. Marincek, S. Gay, D. Weishaupt. *Radiology*. **2004**, *233(1)*, 149-157.

[90] J. D. Collins, A. R. Padhani. *IEEE Eng Med. Biol. Mag*. **2004**, *23(5)*, 65-83.

[91] S. G. Ruehm, C. Corot, P. Vogt, S. Kolb, J. F. Debatin. *Circulation*. **2001**, *103(3)*, 415-422.

[92] B. W. Veldhuis, S. Floris, P. H. Meide van der, I. M. Vos, H. E. Vries, C. D. Dijkstra, P. R. Bar, K. Nicolay. *J. Cereb Blood Flow Metab*. **2003**, *23(9)*, 1060-1069.

[93] G. J. Strijkers, W. J. M. Mulder, *et al*. *Anti-Cancer Agents in Medicinal Chemistry (Formerly Current Medicinal Chemistry - Anti-Cancer Agents)*. **2003.** *7(3),* 291-305.

[94] P. Caravan, J. J. Ellison, T. J. McMurry. R. B. Lauffer. *Chem Rev*. **1999**. *99(9)*, 2293-2352.

[95] K. M. Ward, A. H. Aletras, R. S. Balaban. *Journal of Magnetic Resonance*.**2000**, *143(1)*, 79-87.

[96] S. Aime, C. Carrera, C. D. Delli, C. S. Geninatti, E. Terreno. *Angew. Chem. Int. Ed Engl.* **2005,** *44(12)*, 1813-1815.

[97] M. P. Ledbetter, C. W. Crawford, A. Pines, D. E. Wemmer, S. Knappe, J. Kitching, D. Budker. *Journal of Magnetic Resonance*. **2009**, *199*, 25-29.

[98] K. S. Lee, M. Mossle, *et al*. *Magnetic Resonance*. **2005**, *53(1)*, 9-14.

[99] S. K. Lee, M. Möβle, W.R. Myers, N. Kelso, A.H. Trabesinger, A. Pines, J. Clarke. Magnetic Resonance. **2005**, *53*, 9-14.

[100] S. Ruangchaithaweesuk, D. S. Yu, N. C. Garcia, L. Yao, S.-J. Xu. Journal of Magnetic Resonance. **2012**, *223,* 20-24.

[101] T. Neuberger, B. Schopf, H. Hoffman, M. Hoffman, and B. von Rechenberg. *Journal of Magnetism and Magnetic Materials*. **2005**, *293(1)*, 483-496.

[102] A. S. Lubbe, C. Bergemann, H. Riess, F. Schriever, P. Reichardt, K Possinger, M. Matthias, B. Dorken, F. Hermann, R. Gurtler, P. Hohenberger, N. Haas, R. Sohr, B. Sander, D. Ohlendorf, W. Hunt, and D. Huhn, *Cancer Research.* **1996**, *56(20),* 4686-4693.

[103] N. Kohler, C. Sun, J. Wang, M. Zhang. *Langmuir.* **2005**, *21(19),* 8858-8864.

[104] H.-H. Yang, S.-Q. Zhang, X.-L. Chen, Z.-X. Zhuang, X.-R. Wang. *Analytical Chemistry.* **2004**, *76(5),* 1316-1321.

[105] P. Majewski and B. Thierry. *Critical Reviews in Solid State and Materials Sciences.* **2007**, *32(3-4),* 230-215.

[106] P. Tartaj, M. del Puerto Morales, S. Veintemillas-Verdaguer, T. Gonzalez-Carreno, and C. J. Serna. *Journal of Physics D: Applied Physics.* **2003**, *36(13),* R182-R187.

[107] J. S. Kim, T. J. Yoon, K. N. Yu, B. G. Kim, S. J. Park, H. W. Kim, K. H. Lee, S. B. Park, J. K. Lee, and M. H. Cho. *Toxicological Sciences.* **2006**, *89(1),* 338-347.

[108] L. Chaiet and F. J. Wolf. *Archives of Biochemistry and Biophysics.* **1964**, *106*, 1-5.

[109] N. M. Green. *Advances in Protein Chemistry.* **1975**, *29*, 85-133.

[110] P. R. Langer, A. A. Waldrop, D. C. Ward. *Proceedings of the National Academy of Sciences U.S.A.* **1981**, *78*, 6633-6637.

[111] P. C. Weber, D. H. Ohlendorf, J. J. Wendoloski and F. R. Salemme. *Science, New Series*. **1989,** *243 (4887*), 85-88.

[112] M. Fujinaga and R. Read. *Journal of Applied Crystallography*. **1987**, *20*, 517.